J. Fluid Mech. (1992), *vol.* 240, *pp.* 433–468
Printed in Great Britain

Numerical studies of natural transition in a decelerating boundary layer

By KYUNG-SOO YANG[1], PHILIPPE R. SPALART[2]† AND JOEL H. FERZIGER[1]

[1] Department of Mechanical Engineering, Stanford University, Stanford, CA 94305, USA
[2] NASA-Ames Research Center, Moffett Field, CA 94035, USA

(Received 15 January 1991 and in revised form 5 December 1991)

Laminar–turbulent transition in the decelerating boundary layer of Gad-el-Hak *et al.* (1984) is studied by solving the incompressible, time-dependent, three-dimensional Navier–Stokes equations numerically. The temporal and spatial evolution of the experimental flow structures is approximated with spatial periodicity and temporal evolution while maintaining mean-velocity profiles appropriate to the spatially-developing flow. Other than the mean flow, the initial flow fields include only small-amplitude white random noise. This and the large streamwise and spanwise dimensions of the numerical domain allow unstable waves to be selected by the dynamics, instead of being imposed arbitrarily as in previous numerical studies. In that sense, the transition is natural. In the early stages of transition, two-dimensional and slightly oblique waves grow rapidly owing to inflexional instability. Their subsequent nonlinear interactions trigger the breakdown and create a pattern of Λ vortices. The patterns of Λ vortices are more irregular than those found in ribbon-induced transition. The tips of the Λ vortices are rarely aligned with the flow direction, and they appear in local patches, consistent with the experimental visualizations of Gad-el-Hak *et al.* A simple model based on the interference of multiple modes of instability accounts for these features, but the specific pattern of Λ vortices depends on the random content of the initial flow field. A simulation of the later stages of transition is performed with higher numerical resolution, showing that the 'naturally-born' Λ vortices undergo breakdown processes similar to those of their ribbon-induced counterparts.

1. Introduction

Laminar–turbulent transition is a transient stage of a flow field from 'regular and smooth' laminar flow to 'random and chaotic' turbulent flow. The experiment of Reynolds in 1883 established that such a transition stage occurs prior to a laminar flow becoming fully turbulent. It was also shown that transition occurs at a dimensionless number (now called 'Reynolds number') above some threshold value.

For the purpose of controlling engineering flows, it is important to understand the mechanisms active in this transient phenomenon. Suppression or triggering of transition is used when either laminar or turbulent flow is desirable in a specific application. For example, laminar flow is favoured to reduce drag on an airfoil. On

† Present address: Boeing Commercial Airplane Group, P.O. Box 3707, MS 7H-96, Seattle, WA 98124-2207, USA.

the other hand, turbulence is desirable in combustion or chemical mixing, or in preventing separation.

In spite of the tremendous effort dedicated to laminar–turbulent transition over several decades, the understanding of transition is far from complete. Laminar–turbulent transition is a complicated phenomenon that depends not only on the Reynolds number, but on other factors such as pressure gradient, free-stream disturbance level and wall roughness, and becomes highly nonlinear in its later stages. This combination of numerous parameters and nonlinearity has been a major obstacle to satisfactory understanding of laminar–turbulent transition.

In boundary layers, the linear theory describes the very early two-dimensional evolution of disturbances, hereafter called the 'primary instability', quite well, but fails to explain their later development. It was natural that, as the next step, investigations should focus on the development of three-dimensional disturbances, now attributed to a 'secondary instability'. Many vibrating-ribbon experiments (Klebanoff, Tidstrom & Sargent 1962; Kovasznay, Komoda & Vasudeva 1962; Saric, Kozlov & Levchenko 1984) were performed to study the production of three-dimensional structures and their subsequent deformation. Theories based on nonlinear interaction of wave triads (Craik 1971), and on the secondary instability in the presence of a finite-amplitude two-dimensional wave (Orszag & Patera 1983; Herbert 1985) have been developed. Several types of breakdown (patterns of Λ vortices) were identified and experimentally verified (Thomas 1983; Saric *et al.* 1984; Kachanov & Levchenko 1984). Herbert (1988) reviewed the secondary instability. Little work has been done on stages beyond the onset of secondary instability owing to the highly nonlinear and intermittent nature of the flow. It is believed that these later stages of transition in boundary layers involve the formation of thin but intense shear layers (called 'high-shear layers'), multiple spikes, hairpin vortices and streaky structures near the wall, and finally the formation of turbulent bursts. There are also 'bypass' mechanisms that avoid some of the stages in this scenario.

Most numerical simulations of transition have been done on geometrically-simple flows such as plane channel flows and flat-plate boundary layers. Wray & Hussaini (1984) performed a numerical study on the breakdown stage of transition in the Blasius boundary layer. Using a finite-amplitude two-dimensional wave and a pair of finite-amplitude oblique waves as initial conditions, they accurately simulated the multi-spike stages. Their results are consistent with the experimental data of Kovasznay *et al.* (1962). Laurien & Kleiser (1985) conducted similar simulations; they included subharmonic-type breakdown which Wray & Hussaini (1984) did not consider. They also studied active transition control by employing anti-phased suction/blowing at the wall. Spalart & Yang (1987, hereinafter referred to as SY) numerically studied ribbon-induced transition in Blasius flow. Besides a finite-amplitude two-dimensional Tollmien–Schlichting (TS) wave, they used small-amplitude random noise as a background disturbance, and simulated the early stages of transition. Their results are in good agreement with the experiments of Saric *et al.* (1984).

In the numerical simulations mentioned above, it was assumed that the mean velocity depends on only y and t, and that disturbances are periodic in x and z. Therefore, the disturbances grow in time, in contrast to laboratory experiments or practical flows, in which they grow in both space and time. This 'temporal' approach can be related to the spatial approach only when the growth rates of the disturbances are small, and the mean flow is treated as parallel (Gaster 1962). Fasel (1976) studied spatially-developing instabilities in two-dimensional flat-plate boundary layers.

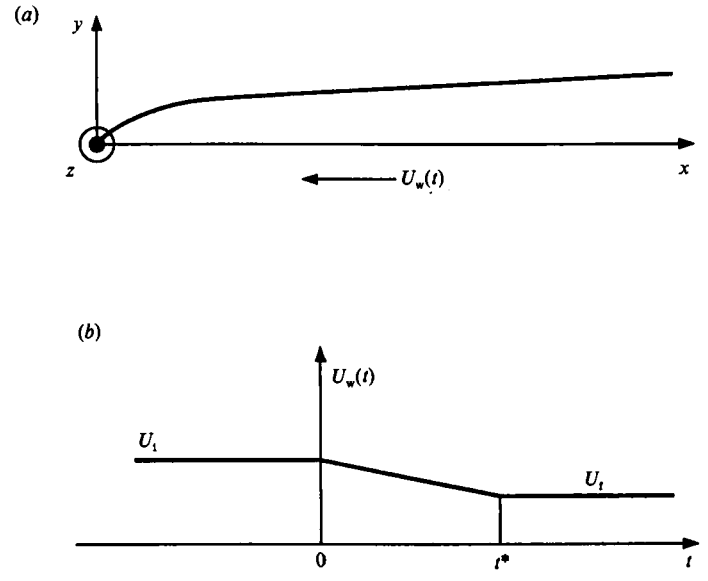

FIGURE 1. Schematic drawing of a decelerating boundary layer. (*a*) Configuration of the experiment of Gad-el-Hak *et al.* (1984). (*b*) Velocity of the plate.

Fasel, Konzelmann & Rist (1986) extended the spatial approach to three-dimensional disturbances; the disturbances remain periodic in the spanwise direction. Their approach represents the experimental situation more accurately, but the numerical difficulties are also more severe.

Ribbon-induced transition has been a prevalent subject in transition research because it involves a clean and reproducible mechanism leading to transition. Although the understanding of ribbon-induced transition is fundamental, it is also different from practical situations in that the primary instability is 'isolated periodic' (Gaster 1980) and arbitrarily chosen. The next step should be to investigate a route to transition in which unstable waves are naturally selected and modulated. Natural transition is more difficult and expensive to simulate than forced (or controlled) transition, such as ribbon-induced transition. A larger computational box, more computing time, and more refined grids are needed to follow instability mechanisms which are not known in advance.

An ideal flow to start studying natural transition is Blasius flow. However, its simulation is very difficult owing to the problems listed above. The decelerating boundary layer provides an alternative. Deceleration generates a strong inflexional instability which causes transition to occur more quickly than in Blasius flow (Gad-el-hak & Davis 1982; Gad-el-Hak *et al.* 1984, hereinafter referred to as GH), thus facilitating numerical simulation. This flow is also closer to a time-developing flow because transition occurs almost simultaneously all over the plate. Therefore, this problem may be one of the more suitable boundary-layer problems that can be addressed by a temporal code. The large growth rates obviate the need for considering non-parallel effects. The review article by Kleiser & Zang (1991) gives a further discussion on spatial and temporal simulations.

For these reasons, a decelerating flat-plate boundary layer was chosen for numerical simulation. Experiments on such flows were done by Fales (1955) and Hegarty (1958). GH performed an experiment on the boundary layer on a

decelerating flat plate in a towing tank. They observed the evolution of strong two-dimensional waves, followed by three-dimensional distortion, Λ-shaped vortices and, finally, breakdown to turbulence. These processes occurred without artificially introduced waves.

The physical configuration of the present study and of the GH experiment is depicted in figure 1 (*a*). A flat plate of finite length, L, moves in stationary fluid with a velocity, U_w, which varies with time, t. Initially, the velocity is U_i; it then decreases linearly to a final constant velocity, U_f (figure 1*b*). The deceleration period is denoted by t^*.

The three dominant parameters are $R_{\delta_0^*}$, the Reynolds number based on the initial displacement thickness (δ_0^*) at a given streamwise location, t^*U_i/δ_0^*, the non-dimensionalized deceleration period which measures the rapidity of the deceleration, and U_f/U_i, the ratio of the final velocity to the initial velocity which represents the strength of the deceleration. The laminar flow is not self-similar, but the mean velocity profiles at a given time collapse onto a single curve if the three parameters are matched.

2. Mathematical and numerical considerations

2.1. *Assumptions*

We make the approximation that the mean flow depends only on y and t, and that the disturbances are periodic in x and z and amplify in time. Under these assumptions, Fourier methods can be employed in the streamwise and spanwise directions. The effects of these assumptions are subtle and hard to evaluate. A rough estimate can be made by comparing the computational results with experiments or simulations of spatially-developing flow. Fasel *et al.* (1986) studied instabilities in a spatially-developing (only in the streamwise direction) boundary layer, and found good agreement with a temporal computation in the linear stage of transition. Temporal simulations by Wray & Hussaini (1984) of the breakdown stage of transition in Blasius flow also showed most of the essential features of the experiment of Kovasznay *et al.* (1962). Therefore, the use of the temporal approach is reasonable but care must be taken in evaluating the results.

Boundary layers are more difficult than channel flows to simulate. The effect of increasing thickness on linear stability has been studied by Barry & Ross (1970), Ling & Reynolds (1973), Saric & Nayfeh (1975), and others. Although their approaches are different, and non-parallel stability theory is highly controversial, their conclusions are that the boundary layer is slightly less stable when the non-parallel correction is included (i.e. the critical Reynolds number is less than that of the parallel flow) and that the non-parallel effect diminishes as the Reynolds number increases. Furthermore, the GH experiment reveals several wavelengths in x and z which appear to be at the same stage of breakdown. This suggests that periodic conditions in x and z should be adequate, and more so in this flow than in Blasius flow.

Under these two basic assumptions, our numerical simulations will be of temporally growing boundary layers. However, we will approximate spatially developing flows as closely as possible by making corrections; we call this a 'pseudo-spatial approach'. The details are discussed below.

2.2. *Spectral formulation*

The full time-dependent incompressible Navier–Stokes equations with appropriate initial and boundary conditions are solved under the assumptions of §2.1. They are

$$\frac{\partial \boldsymbol{u}}{\partial t} - \boldsymbol{u} \times \boldsymbol{\omega} = -\frac{1}{\rho} \nabla [p + \tfrac{1}{2}(\rho \boldsymbol{u} \cdot \boldsymbol{u})] + \nu \nabla^2 \boldsymbol{u} + \boldsymbol{F}, \tag{2.1}$$

$$\nabla \cdot \boldsymbol{u} = 0, \tag{2.2}$$

$$\boldsymbol{u} = \boldsymbol{0} \quad \text{at } y = 0, \tag{2.3}$$

$$\boldsymbol{u} \to \boldsymbol{U}_\infty(t) \quad \text{as } y \to \infty. \tag{2.4}$$

Here, $\boldsymbol{F}(y, t)$ is a forcing function which will be discussed in later sections, and $\boldsymbol{U}_\infty(t)$ is the velocity far from the plate. Initial conditions are given below.

We use a weak formulation similar to Leonard & Wray's (1982), except for the choice of weight functions. This is described in detail elsewhere (Spalart, Moser & Rogers 1991). Spectral methods, which have very high accuracy for smooth flow fields, are employed in all three directions. Since we deal with an incompressible flow in which a disturbance at one point in the flow field is instantaneously felt throughout the entire flow field via pressure interactions, the global character of spectral methods seems appropriate. The assumption of periodic disturbances allows the use of Fourier expansions in the streamwise and the spanwise directions. In the normal direction, combinations of Jacobi polynomials are used (Spalart *et al.* 1991).

2.3. *Initial flow field*

Time-integration requires an initial flow field. In a laboratory, there exist disturbances from various sources. They can be classified into two groups – irrotational (e.g. sound) and vortical disturbances (e.g. free-stream turbulence). It is not a trivial task to model these disturbances in the numerical simulations.

In the present study, the initial flow field contains only small-amplitude random disturbances and the mean flow. The disturbances are obtained from a random-number generator, uniform in x and z, and tapering to 0 at the wall and in the free-stream. They are added only at the beginning of simulation. This is far from a perfect duplication of the disturbances in the laboratory flow field, which are probably continuous in both space and time, but it does activate all the modes that are capable of a large amplification. It should be noted that most other simulations (Kleiser & Laurien 1985; Wray & Hussaini 1984; Biringen 1984) did not include noise-like disturbances at all.

2.4. *Computational resources*

All computations were carried out on the Cray X-MP/48 at the NASA Ames Research Center. Numerical simulations of the early stages of transition use $64 \times 40 \times 48$ grid points in x-, y- and z-directions, respectively. A typical run takes about 650 timesteps, each requiring about 4 s of CPU time. In the case of later stages of transition, the resolution is successively refined (by means of spectral interpolation); the maximum number of grid points used was $96 \times 128 \times 512$. Owing to the large amount of data, it is necessary to hold the data on a secondary storage device, and to load small sections of it into the core memory to be processed.

3. The decelerating two-dimensional boundary layer

This section describes simulations of an incompressible two-dimensional decelerating laminar boundary layer on a flat plate of finite length. A two-dimensional

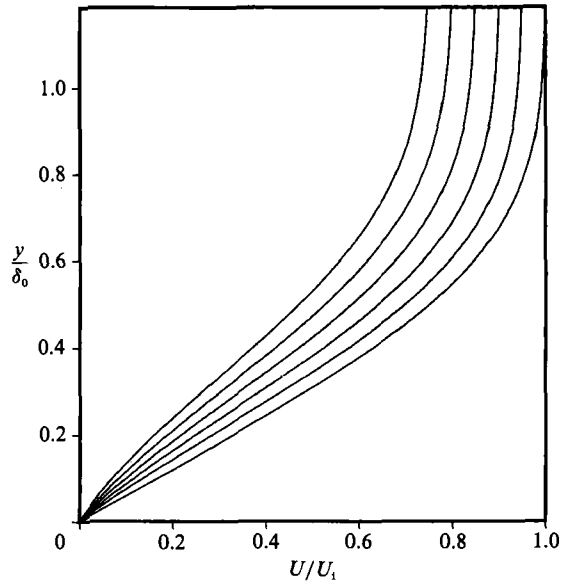

FIGURE 2. Mean-velocity profiles obtained from the two-dimensional code, $R_{\delta_0^*} = 1090$, $t^*U_1/\delta_0^* = 733$, $U_f/U_1 = 0.75$, $\Delta t/t^* = 0.2$.

unsteady boundary-layer code was written and tested, and used to provide the mean velocity profiles for the three-dimensional simulations. Details will be given in §4. It is also helpful to study the linear stability characteristics of this flow before performing full three-dimensional simulations.

3.1. *Formulation and numerical procedure*

The configuration of the GH experiments is depicted in figure 1 (*a*). The laminar flow is two-dimensional. For incompressible flows, the decelerating-plate problem and the problem in which the plate is stationary and the free stream decelerates generate the same flow (see Appendix). Furthermore, in the experiment, all flow variables were measured relative to the plate. For these reasons, we simulate the decelerating-free-stream problem.

Under the boundary-layer approximations, the governing equations and initial and boundary conditions are

$$\frac{\partial U}{\partial t}+U\frac{\partial U}{\partial x}+V\frac{\partial U}{\partial y}=\frac{\mathrm{d}U_\infty}{\mathrm{d}t}+\nu\frac{\partial^2 U}{\partial y^2}, \tag{3.1}$$

$$\frac{\partial U}{\partial x}+\frac{\partial V}{\partial y}=0, \tag{3.2}$$

$$U=U_{\mathrm{B}}(x,y) \quad \text{at } t=0, \tag{3.3}$$

$$U=V=0 \quad \text{at } y=0, \tag{3.4}$$

$$U\to U_\infty(t) \quad \text{as } y\to\infty, \tag{3.5}$$

where U and V are the velocity components, U_∞ is the streamwise component of the free-stream velocity, and U_{B} is the streamwise velocity in Blasius flow.

Equations (3.1)–(3.5) hold for $x\in[0,L]$. A finite-difference method is employed in x, and a spectral method in y (using some of the basis functions of the direct-simulation code). Uneven grid spacing is used in the streamwise direction for better

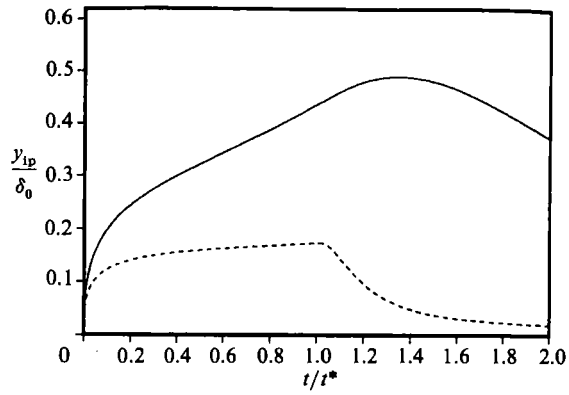

FIGURE 3. Migration of the inflexion point, $R_{\delta_0^*} = 1090$, $t^*U_1/\delta_0^* = 733$, ——, $U_f/U_1 = 0.56$, ---, $U_f/U_1 = 0.94$.

t/t^*	$k_x\delta^*$	$k_x c_i$
0.0	0.25	0.4853
0.2	0.26	1.022
0.4	0.27	1.281
0.6	0.27	1.346
0.8	0.28	1.381
1.0	0.29	1.448

TABLE 1. Growth rates of the most unstable waves at $x/L = 0.37$, where c_i is the imaginary part of the phase velocity

accuracy near the leading edge. The streamwise derivative $(\partial/\partial x)$ is approximated by second-order finite differencing except at the outflow, where upwind differencing is used instead. The inflow is assumed to be the instantaneous Blasius flow (based on $U_\infty(t)$) at the first x station ($0.04L$). To integrate (3.1) in time, the Crank–Nicolson scheme is applied to the viscous term, and a third-order Runge–Kutta scheme is applied to the convective terms.

3.2. *Linear stability analysis*

In this section, results obtained with the two-dimensional code for the decelerating boundary layer are discussed. The flow parameters are $R_{\delta_0^*} = 1090$, $t^*U_1/\delta_0^* = 733$, and $U_f/U_1 = 0.75$, as in the experiment. Figure 2 shows the velocity profiles at $x/L = 0.37$ and at time intervals of $\Delta t/t^* = 0.2$. Except for the initial Blasius profile, these profiles are inflexional. The migration of the inflexion point is given in figure 3 for two values of the deceleration strength, $U_f/U_1 = 0.56$ and $U_f/U_1 = 0.94$, while the other parameters remain unchanged. The stronger the deceleration, the further the inflexion point migrates from the wall. In any case, it returns to the wall when the profile approaches the final Blasius profile. Since the intermediate profiles are inflexional, we expect the flow to be very unstable (Drazin & Reid 1981). Table 1 gives the growth rates of the most unstable waves of each profile in figure 2. They were calculated using a linearized version of the three-dimensional code assuming quasi-steady and parallel mean flow. At the end of the deceleration, the growth rate reaches a maximum about three times as large as that of the Blasius profile. This allows the possibility of simulating natural transition without excessive computation times. The strong growth rate eliminates the need for the initial strong two-

dimensional TS wave, which was included in previous numerical simulations in order to duplicate the vibrating-ribbon technique of the experiments.

4. Simulations of the early stages of transition

4.1. *Formulation*

Since the stability characteristics are very sensitive to the shape of the mean-velocity profile, it is important that this profile be correct especially in a simulation of the early stages of transition. Such a simulation is long enough for the primary instability to produce a large amplification. Therefore, it is necessary in a temporal simulation to modify the x momentum equation to maintain the correct mean-velocity profile (see SY). The modified x momentum equation is

$$\frac{\partial u}{\partial t}+\boldsymbol{u}\cdot\boldsymbol{\nabla}u=-\frac{1}{\rho}\frac{\partial \tilde{p}}{\partial x}+\nu\nabla^2 u+\frac{\partial U_{2\mathrm{D}}}{\partial t}-\nu\frac{\partial^2 U_{2\mathrm{D}}}{\partial y^2}, \tag{4.1}$$

where $\tilde{p}$ is the pressure fluctuation and $U_{2\mathrm{D}}(x_0, y, t)$ denotes the velocity profile generated by the two-dimensional unsteady boundary-layer code, described in §3, at a streamwise location x_0. The last two terms are artificially added to the usual Navier–Stokes equations. Therefore, for this problem, the forcing term $\boldsymbol{F}$ in (2.1) is

$$\boldsymbol{F}=\begin{pmatrix}\dfrac{\partial U_{2\mathrm{D}}}{\partial t}-\nu\dfrac{\partial^2 U_{2\mathrm{D}}}{\partial y^2}\\ 0\\ 0\end{pmatrix}.$$

Averaging (4.1) in x and z, in the manner of Reynolds-averaging, yields

$$\frac{\partial U}{\partial t}-\frac{\partial \tau}{\partial y}=\nu\frac{\partial^2 U}{\partial y^2}+\frac{\partial U_{2\mathrm{D}}}{\partial t}-\nu\frac{\partial^2 U_{2\mathrm{D}}}{\partial y^2}. \tag{4.2}$$

Equation (4.2) with the initial condition, $U(y, 0) = U_{2\mathrm{D}}(x_0, y, 0)$, shows that the mean-velocity profile ($U(y, t)$) will equal $U_{2\mathrm{D}}$ in the early stages of transition, when the Reynolds stress (τ) is small. We used the two-dimensional code to compute $U_{2\mathrm{D}}$ at a given streamwise location at a set of discrete times. The velocity profiles at intermediate times were obtained by linear interpolation.

4.2. *Choice of parameters*

To match the experiment, we chose the 'numerical' test section to be at $x = 0.62$ m ($L = 2.7$ m), the period of deceleration to be $t^* = 5$ s, and the initial and final velocities to be $U_\mathrm{i} = 0.4$ m/s and $U_\mathrm{f} = 0.3$ m/s. Although the experimental visualization pictures were taken at $x = 1.0$ m by GH, the two-dimensional profiles are taken at $x = 0.62$ m. The reason is given in §4.4.2. Using these values, the key parameters are $R_{\delta_0^*} = 856$, $t^* U_\mathrm{i}/\delta_0^* = 935$, and $U_\mathrm{f}/U_\mathrm{i} = 0.75$. At this rate of deceleration, flow separation does not occur. In the experiment, the plate was towed at the constant initial velocity before the deceleration in order to eliminate start-up unsteadiness and to establish a Blasius profile over the whole plate. Background disturbances are simulated by including small-amplitude white random noise at the beginning of the simulation. In order to establish realistic waves, we maintained the initial Blasius profile for a time t^*, namely 5 s, before decelerating the flow. As a result, at the start of deceleration, the unstable modes have more energy than the other modes. This represents the disturbances in the developed Blasius flow more accurately than unprocessed white random noise.

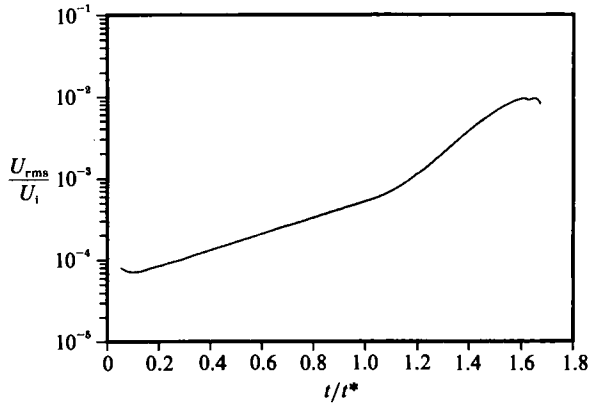

FIGURE 4. Growth of the most unstable two-dimensional wave obtained with the full simulation, $k_x \delta_0^* = 0.294$.

t/t^*	Theory	Simulation
0.4	0.47	0.47
1.2	1.11	1.11
1.4	1.23	1.20
1.5	1.25	0.86

TABLE 2. Comparison of calculated growth rates with quasi-steady theoretical ones ($x = 0.62$ m)

The choice of the computational box size is somewhat arbitrary. It must be large enough to contain the essential features of the flow. The smallest non-dimensional wavenumbers in the streamwise and the spanwise directions were empirically chosen to be $k_{x_0} \delta_0^* = 0.0420$ and $k_{z_0} \delta_0^* = 0.0672$, respectively. With these values, the streamwise and the spanwise sizes of the computational box are about 150 times and 93 times the initial displacement thickness at $x = 0.62$ m (δ_0^*), respectively. Based on the wavelengths predicted by linear theory one can expect 5–7 two-dimensional waves to be contained in the computational domain. The grid was relatively coarse ($64 \times 40 \times 48$) but sufficient for the early stages. For instance, it could resolve 21 waves in the x-direction.

4.3. *Code verification*

Figure 4 shows the growth of the most unstable two-dimensional wave obtained with the full simulation, which corresponds to $k_x \delta_0^* = 0.294$ (k_x is the dimensional streamwise wavenumber). Figure 4 gives the maximum value (with respect to y) of the modal $U_{\rm rms}$ (modulus of the Fourier coefficient) as a function of time. In the beginning, the behaviour is linear. The small initial dip, already observed for noise-like disturbances (see SY), is due to the decay of fluctuations not belonging to the most unstable eigenmode. Once established, the eigenmode grows exponentially at a constant rate. Deceleration starts at $t/t^* = 1.0$. The growth rate increases during deceleration as expected from linear theory (table 1). In the linear regime, the growth rate calculated from the full simulation is very close to the value obtained from the Orr–Sommerfeld equation with the corresponding mean-velocity profile; this region corresponds to the first two rows of table 2. When the amplitude becomes large, nonlinear interactions occur and the growth rate deviates from the Orr–Sommerfeld value as shown in the last two rows of table 2. The end of the simulation shows a tendency towards turbulent behaviour.

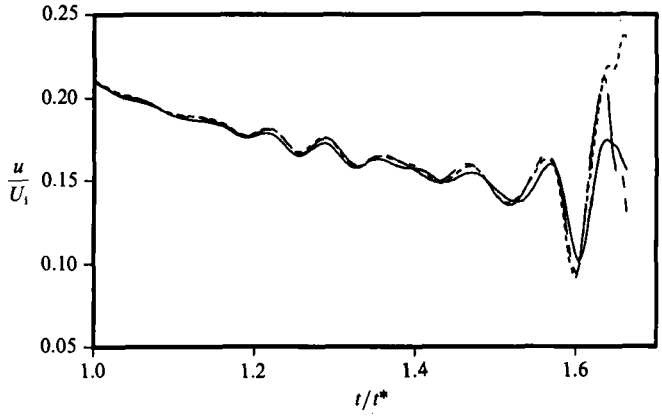

FIGURE 5. Spanwise variations of the instability waves.

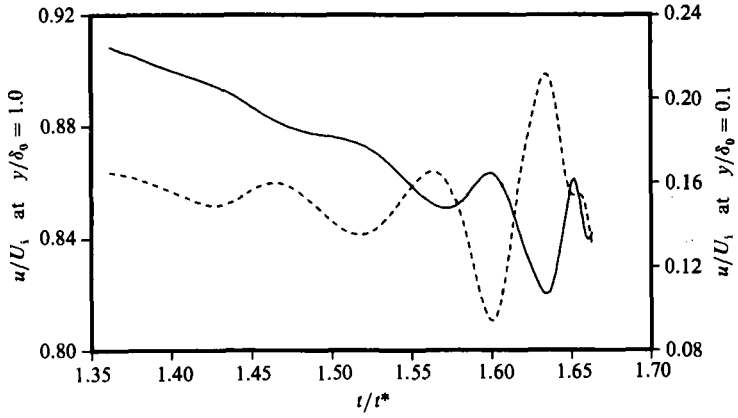

FIGURE 6. Instantaneous streamwise velocity at two different vertical locations. ——, $y/\delta_0 = 1.0$; ---, $y/\delta_0 = 0.1$.

4.4. *Results and discussion*

4.4.1. *Point values*

Streamwise-velocity histories at three equispaced spanwise locations and the same streamwise location are given in figure 5. The three 'numerical' probes are at $x = 1.0$ m and $y = 0.1\delta_0$ where δ_0 is the initial boundary-layer thickness and $2\delta_0$ apart in the spanwise direction. This matches the GH experiment. The decrease of the mean velocity is due to the deceleration. The fluctuations are roughly sinusoidal, which suggests that they are manifestations of the primary instability. The phases at the three locations are almost identical until about $t/t^* = 1.32$, and only slightly different afterwards. This implies that two-dimensional and slightly oblique waves dominate in the early stages of transition. The experiment shows the same degree of two-dimensionality. See figure 8 in GH (1984). After $t/t^* = 1.6$, the three velocities are significantly different in magnitude and phase, which indicates the onset of three-dimensional disturbances amplified by the secondary instability.

Figure 6 shows the streamwise velocity at two different vertical locations $y = 0.1\delta_0$ and $y = \delta_0$ (again matching the GH experiment), at the same streamwise and spanwise locations. The mean velocity at $y = \delta_0$ decreases consistently. On the other hand, the mean velocity at $y = 0.1\delta_0$ decreases in the beginning, but increases later.

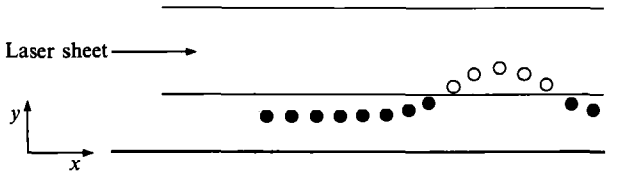

FIGURE 7. Schematic drawing of experimental flow visualization.

In the laminar flow, the mean velocity decreases at both locations owing to the applied deceleration (figure 2). The transitional flow, however, shows a different trend as the instability brings high-momentum fluid downwards, and low-momentum fluid upwards. Moreover, the two signals have opposite phases, indicating that the perturbation has a vortical nature. The experiment indicates the same trends, see figure 12 in GH (1982).

4.4.2. *Flow visualization*

A common way of studying flow structures is via flow visualization with passive particles. In experiments, various methods are available depending on the flow under study. GH used a fluorescent dye as a marker. They released the dye at the wall, and the lifted portion of it was illuminated by a laser sheet (figure 7). In order to mimic this method, we released 9000 passive particles, uniformly in x and z over the computational domain, at $y = 0.197\delta_0$ at the beginning of deceleration, and then subsequently plotted the (x,z)-positions of particles whose y-position was above $0.202\delta_0$. These y-values were chosen empirically and lie between the main and secondary Λ vortices near the wall (this will become clear in §4.4.3). Thus, the following particle visualizations indeed represent the principal Λ structures.

The location of the particles was numerically computed in the same way as in the ribbon-induced transition simulation of SY, using linear interpolation of velocity in space and a Runge–Kutta third-order scheme in time.

Figures 8(*a*)–8(*d*) are four selected frames from the numerical flow visualization. The flow is from bottom to top. No particles are in the frame at the onset of deceleration, because all particles are below the 'numerical laser sheet' (figure 8*a*). Particles are gradually lifted upwards, and confirm that two-dimensional and slightly oblique waves are dominant in the early stages of transition (figure 8*b*). There is a dislocation between two groups of waves. This point will be further discussed in §4.5. The particles form Λ-shaped structures (figure 8*c*), and then breakdown occurs (figure 8*d*). These Λ structures originate not at the test section but somewhere upstream, and translate downstream at the phase velocity of the dominant wave. To correctly simulate this in a time-developing simulation, it is more accurate to use upstream mean-velocity profiles. Recall that much of the wave selection occurs before the deceleration. The two-dimensional wave travels approximately 0.35–0.40 m before the Λ structures develop. Thus, to compare our numerical visualization with the GH experiment at the breakdown stage, we used the mean-velocity profiles at $x = 0.62$ m (whereas their pictures (figure 2) were taken at $x = 1.0$ m). All the non-dimensional parameters reported in this section (except for figure 22) are based on the initial displacement thickness (δ_0^*) at $x = 0.62$ m.

The angle between the two legs of a Λ structure becomes narrower with time, which is an indication of upward and forward motion of the heads, and breakdown first occurs at the tip (figures 8*c* and 8*d*). The timescale of the breakdown is very small compared with the development time of the Λ vortices. Our result is in good agreement with the experimental flow visualization; see figure 2 in GH (1984).

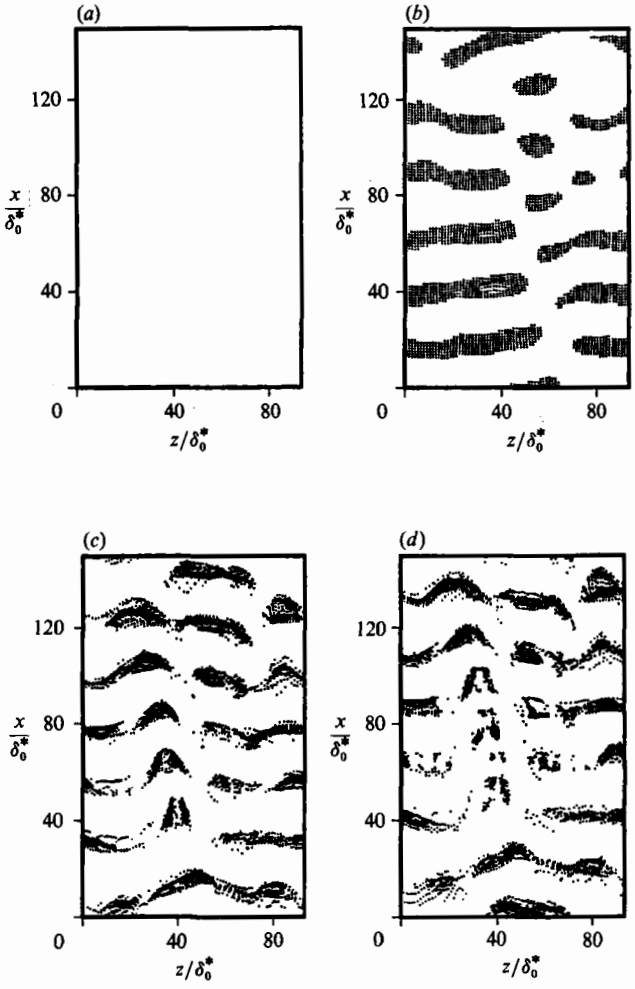

FIGURE 8. Numerical flow visualization with passive particles. (a) $t/t^* = 1.00$; (b) $t/t^* = 1.15$; (c) $t/t^* = 1.61$; (d) $t/t^* = 1.64$.

We can identify further features of the Λ structures common to the experimental and numerical flow visualizations. First, the line connecting the tips of the Λ structures is slightly oblique to the flow direction, the angle being approximately 17° in the simulations and about 20° in the experiment (we should keep in mind that in each case we are describing only one realization of a phenomenon that originates in random noise). See figure 2(*d*) in GH (1984). This contrasts with ribbon-induced transition in Blasius flow (Saric *et al.* 1984; SY) in which the tips of the Λ vortices are always aligned with the flow direction. Secondly, the occurrence of the vortices is localized in space. In some parts of the flow field, no Λ vortices are seen yet. Finally, their streamwise spacing is about 5–$6\delta_0$. Compared with the Λ structures found in ribbon-induced transition, they look more irregular – a feature of natural transition. Consequently, it is harder to control natural transition than forced transition. The obliqueness and localization of the Λ structures will be explained in §4.5.

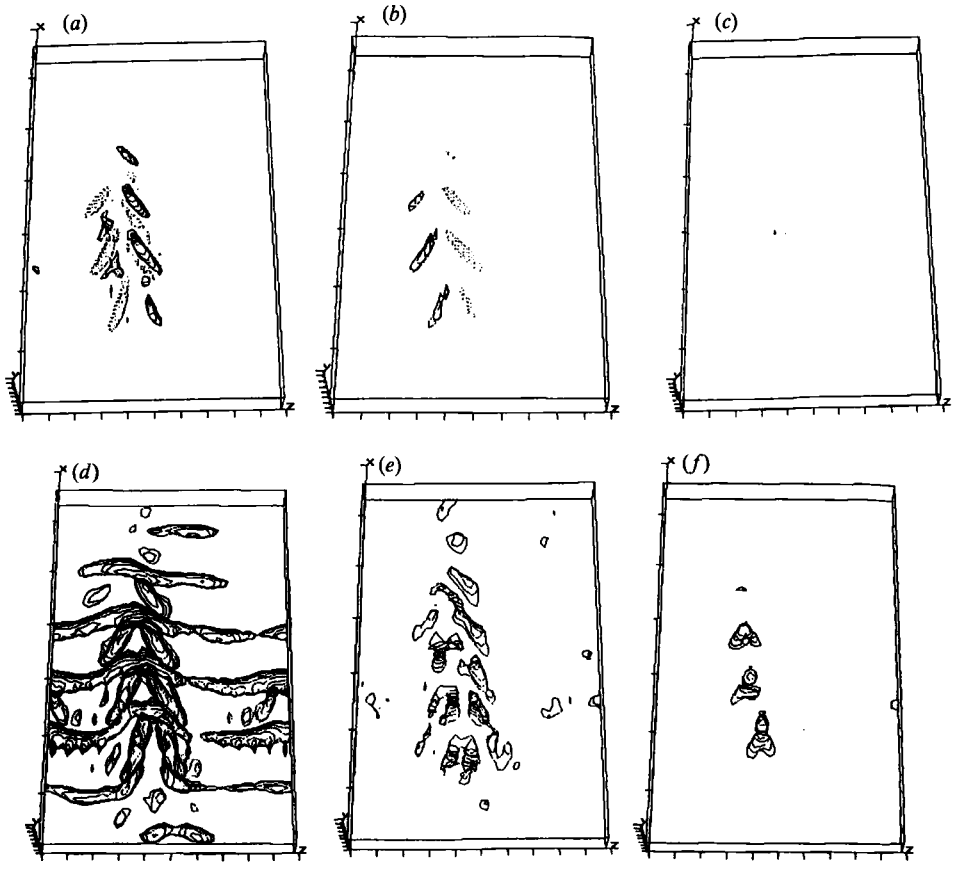

FIGURE 9. Contour plots for ω_x ((*a*), (*b*), (*c*): ——, $-60\ \mathrm{s}^{-1}$; ..., $60\ \mathrm{s}^{-1}$) and ω_z ((*d*), (*e*), (*f*): $-90\ \mathrm{s}^{-1}$) for three y ranges ((*a*), (*d*): 0–$0.12\delta_0$; (*b*), (*e*): 0.19–$0.45\delta_0$; (*c*), (*f*): $0.45\delta_0$ up), $t/t^* = 1.61$.

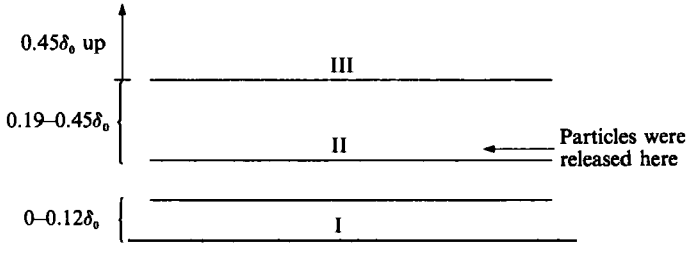

FIGURE 10. Three y ranges for flow visualization (not scaled).

4.4.3. *Vortical structures*

The following questions may be raised. Which parts of the flow structures do the illuminated particles mark? Do the Λ patterns found in the experiment actually represent Λ-shaped vortices? Figure 9 gives streamwise-vorticity (ω_x) and spanwise-vorticity (ω_z) contour plots for three different y-ranges in a perspective view, taken at the same time and streamwise location as figure 8(*c*). Figure 10 illustrates the three y-ranges for which the contour plots were drawn. In this way, vortical structures can be clearly seen without overlapping. The inflexion point of the mean-

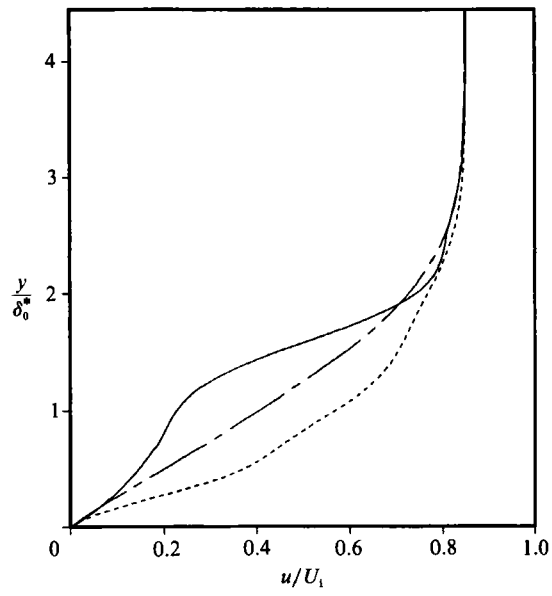

FIGURE 11. Instantaneous streamwise velocity between and outside the legs of the Λ vortices, $t/t^* = 1.61$. ——, 'between' profile; - - -, 'outside' profile; —·—, mean velocity profile.

velocity profile is located at $y = 0.2\delta_0$. The regions marked by solid and dotted lines are regions of large ω_x with opposite signs. Figures 9(*a*) and 9(*b*) show not only the principal Λ vortices but also secondary vortices below them, which are necessary to satisfy the no-slip boundary condition at the wall. The locations of the Λ patterns in figure 8(*c*) and the Λ vortices in figure 9(*b*) match. This supports the usefulness of the visualization technique in locating high-vorticity regions. Even though passive particles need not follow vortical structures in viscous flows, in combination with the laser-sheet technique they do identify these structures for the time period of the GH experiment.

Figures 9(*d*)–9(*f*) show ω_z contour plots for the same y-ranges. Near the wall, large-ω_z regions are due to the secondary Λ vortices and remnants of the TS waves (figure 9*d*). In the intermediate region, the ω_z structures are less coherent (figure 9*e*). It is believed that the velocity field associated with the Λ vortices generates strongly inflexional shear layers (high ω_z regions) above the vortices; these are susceptible to short-wavelength disturbances (Betchov 1960; Greenspan & Benney 1963). The existence of such layers in ribbon-induced transition was demonstrated experimentally by Williams, Fasel & Hama (1984). In spite of the difference in the mechanism producing the Λ vortices, we can locate and identify high-shear layers in our natural transition simulation (figure 9*f*). Note that in this y-range, ω_x is not strong (figure 9*c*), i.e. the high-shear layers are located above the Λ vortices. The arrowhead shape of the high-ω_z regions strongly resembles that found in the experiment of Kovasznay *et al.* (1962). Figure 11 shows instantaneous streamwise-velocity profiles between and outside the legs of a Λ vortex. The 'between' profile reveals the high-shear layer above the vortex. One can expect another inflexional instability (which is localized because the 'outside' profile is stable) to be associated with this high-shear layer.

Vortical structures can also be studied by means of vortex lines. Figures 12(*a*) and 12(*b*) show vortex lines in the computational domain, taken at the same time and at

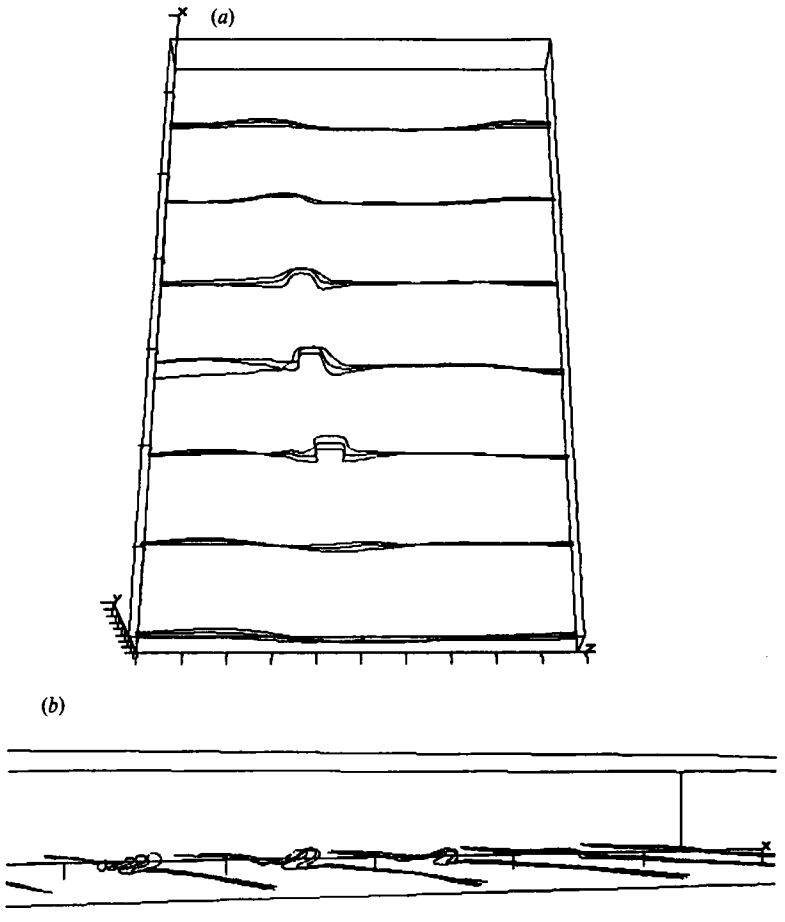

FIGURE 12. Vortex lines, $t/t^* = 1.61$. (*a*) Plan view; (*b*) side view.

the same streamwise location as figure 8(*c*). The flow direction is from bottom to top in figure 12(*a*) and from left to right in figure 12(*b*). Three Λ vortices are clearly seen in figure 12(*a*). The side view (figure 12*b*) shows that they are lifted upwards. The shapes of vortex lines strongly depend upon the starting points used in computing the vortex lines. To generate figure 12, three vertically-equispaced starting points were chosen near the primary vortices (range II in figure 10) at a given streamwise location. The streamwise spacing between bundles of vortex lines is one streamwise wavelength of the most unstable wave (see figure 8*b*).

Figure 12 suggests that the formation and lifting of Λ vortices and subsequent vortex stretching are essential steps in natural as well as forced transition. The ensuing development of the Λ vortices will be studied in §5 with more refined numerical resolution.

4.4.4. *Energy spectra*

Figures 13(*a*)–13(*d*) present the distribution of the kinetic energy over the Fourier modes at four times. The energy of each mode has been integrated in the normal direction. Only half the wave space needs to be shown (the Fourier transform of a real function satisfies a summetry condition). Since we are interested only in modes for

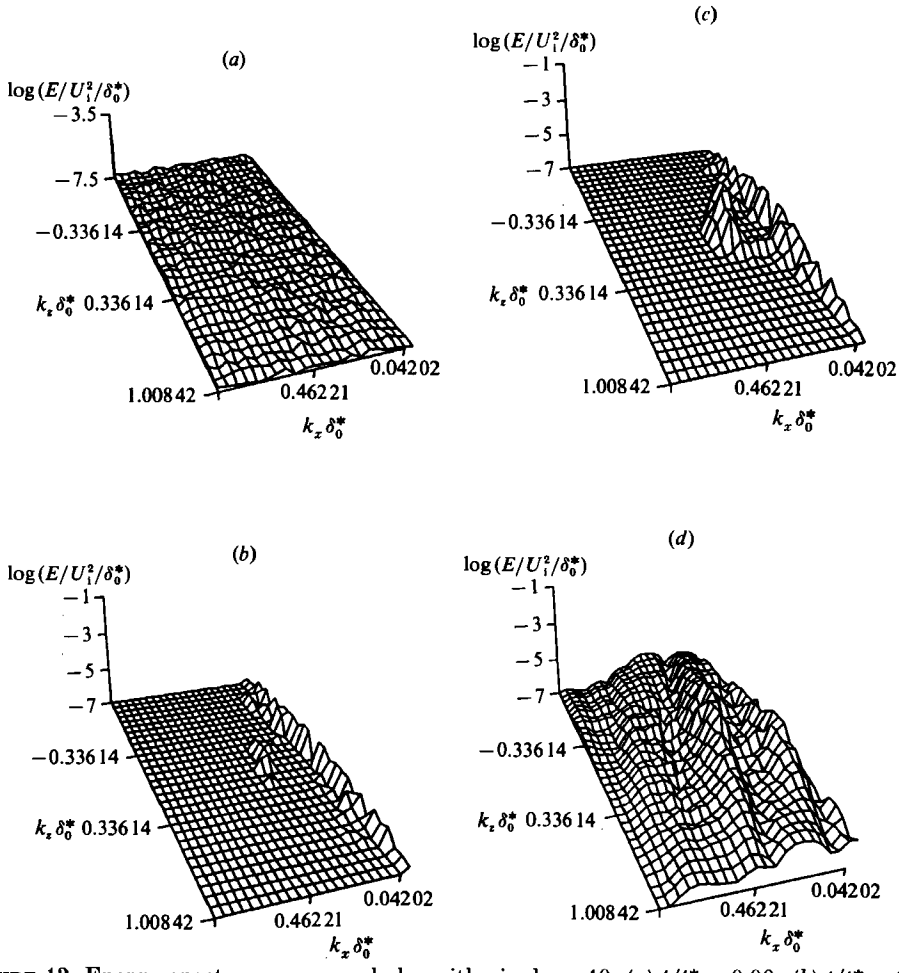

FIGURE 13. Energy spectra, energy scale logarithmic, base 10. (*a*) $t/t^* = 0.00$; (*b*) $t/t^* = 0.97$; (*c*) $t/t^* = 1.40$; (*d*) $t/t^* = 1.61$.

which energy is above a certain level, 'weak' modes are not shown. We also disregard the energy of the mean mode, which is not very meaningful since it is not Galilean-invariant.

Recall that the simulation starts with small-amplitude three-dimensional random noise at $t/t^* = 0$ (figure 13*a*). The noise level was chosen so that at the time of breakdown the total energy in the fluctuations is about the same as in the experiment. Just prior to the initiation of deceleration, certain waves have been selected by the linear mechanism in Blasius flow (figure 13*b*); disturbances without streamwise dependence have significant energy. During deceleration, two-dimensional and slightly oblique three-dimensional waves grow rapidly (figure 13*c*). This is consistent with Squires' theorem (Schlichting 1979). These waves dominate the primary stage of transition. (Recall figure 8*b*.) Later, they interact nonlinearly and fill the spectrum (figure 13*d*). The simulation was stopped at this point for lack of resolution.

Note the ridges in figure 13(*d*), oblique to the k_z-axis. This may be correlated with the fact that the Λ vortices are obliquely aligned. In the simulation of the ribbon-induced transition, the 'mountain tops' are parallel to the k_z-axis (figure 4 in SY),

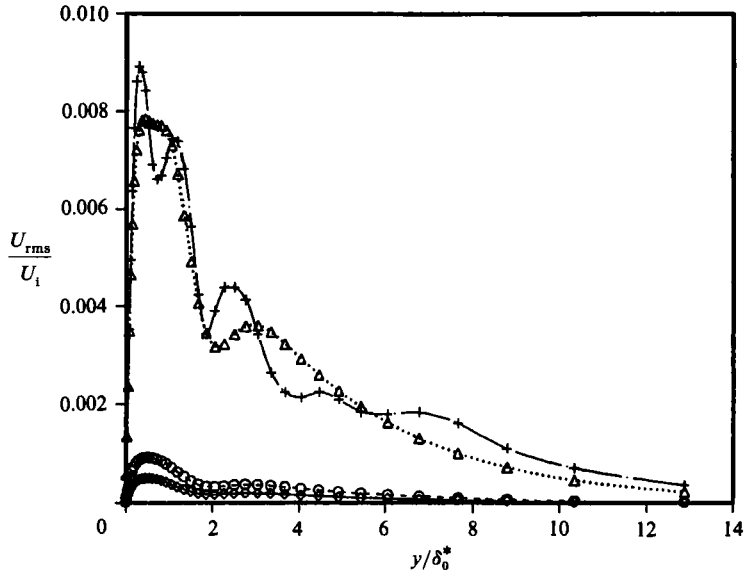

FIGURE 14. Most unstable two-dimensional wave. ◇, $t/t^* = 0.98$; ○, $t/t^* = 1.16$; △, $t/t^* = 1.54$; +, $t/t^* = 1.67$.

resulting in a straightly aligned pattern of Λ vortices. See figures 2(*f*)–2(*h*) in SY. This point will be further discussed in §4.5.

4.4.5. *Role of the most-energetic two-dimensional wave*

Here observe the development of the most unstable two-dimensional wave ($k_x \delta_0^* = 0.294$) during deceleration. Figure 14 shows its magnitude profile at four times. Just before deceleration ($t/t^* = 0.98$), the eigenmode has the typical two-peak shape found in Blasius flow (Herbert 1984). Initially, it grows in a linear fashion, maintaining the two-peak shape. Around $t/t^* = 1.54$, the shape begins to be distorted by nonlinear effects. At $t/t^* = 1.67$, the peak near the wall breaks into two. The dip between the two peaks is located near the critical layer. Similar behaviour has been observed in ribbon-induced transition in channel flows (Nishioka & Asai 1985; Singer *et al.* 1987). Singer *et al.* (1987) studied local energy transfer among triads of waves, and found that the two-dimensional wave loses energy to three-dimensional waves near the critical layer and gains energy above the critical layer, resulting in double peaks near the wall. This again suggests that the most unstable two-dimensional wave (and possibly other strong oblique waves) in natural transition plays a role similar to that of the dominant two-dimensional TS wave in ribbon-induced transition.

4.5. *A model for natural transition*

The structure of a transitional decelerating boundary layer is less regular than that of a transitional boundary layer stimulated by a vibrating ribbon. The GH experiment and the simulations show groups of Λ vortices appearing locally in space, with their tips obliquely aligned with respect to the flow direction.

This kind of unpredictable behaviour is inevitable because there are no 'predominant' modes in the flow field. In this section, a simplified model appropriate to natural transition will be developed. The model explains most of the features observed by flow visualization.

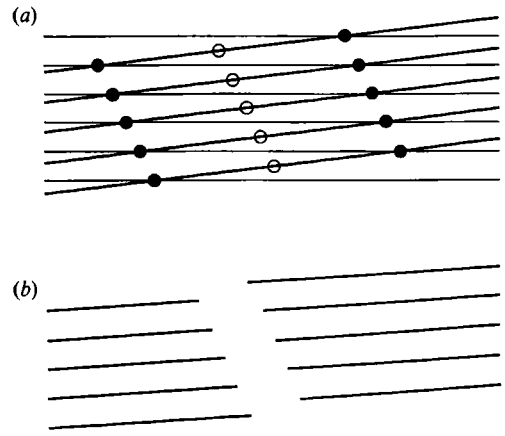

FIGURE 15. Interference between two waves. (a) ●, Enhanced region; ○, cancelled region: (b) resultant.

4.5.1. *Wave interference*

Linear theory shows that more than one wave can grow significantly prior to the beginning of nonlinear interactions. This contrasts with ribbon-induced transition in which a single artifically-introduced two-dimensional TS wave dominates from the outset. In that case, the three-dimensional waves grow with the aid of the primary two-dimensional wave (secondary instability). In natural transition, in addition to two-dimensional waves, slightly oblique waves have a good chance of becoming strong enough to interact with the three-dimensional waves. Figure 13(*c*) shows a good example of this. Let $(k_x\delta_0^*, k_z\delta_0^*)$ indicate a mode whose non-dimensional streamwise and spanwise wavenumbers are $k_x\delta_0^*$ and $k_z\delta_0^*$, respectively. The figure indicates that the two two-dimensional waves, (0.294, 0) and (0.252, 0), are strong as allowed by linear theory (and triggered by the initial random disturbances). However, two oblique waves, (0.252, −0.0672) and (0.252, −0.134) are approximately as strong as the two-dimensional waves.

In the simplest situation, there are just two dominant waves; let us assume they are a two-dimensional wave and an oblique wave. Figure 15(*a*) illustrates such a case with two waves whose streamwise wavenumbers differ only slightly. This is similar to the example mentioned above (figure 13*c*). The solid lines in figure 15(*a*) represent the wave crests. In some parts of flow field (marked by solid circles) the perturbations are enhanced by constructive interference of the two waves, while in other parts of the flow (those marked by open circles) the perturbations are reduced by cancellation of the two waves. Figure 15(*b*) depicts the result. Here, the thick solid lines represent the enhanced regions. Notice that each line is broken, not straight. This may explain the dislocation between two patches of waves observed in figure 8(*b*). It can be further conjectured that the Λ vortices (which will appear in the enhanced regions owing to vortex tilting and stretching) will be obliquely aligned (figure 8*c*). Since there are 'quiet' regions in the flow field, one may expect that the Λ vortices will appear as local patches (figure 8*c*).

4.5.2. *Test of the simple model*

The value of this conjecture can be demonstrated by numerical simulation. For direct comparison with the flow visualizations reported in this section, a simulation containing only one two-dimensional wave (0.294, 0), and one oblique wave (0.252,

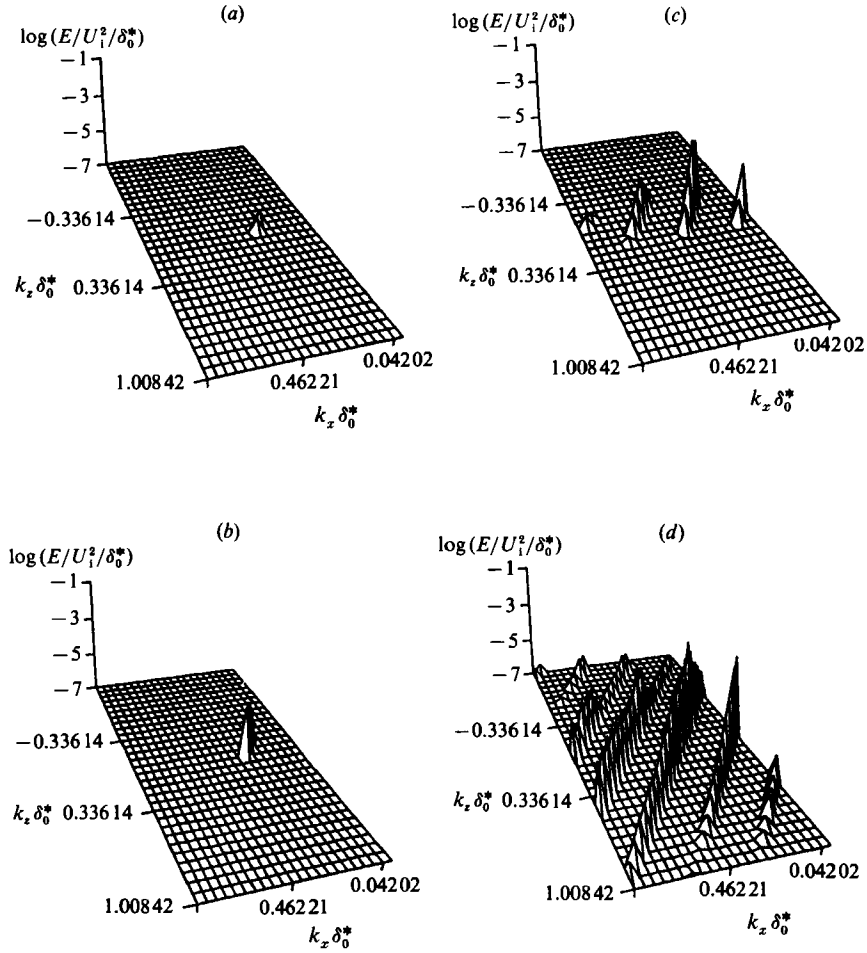

FIGURE 16. Energy spectra for model simulation. (*a*) $t/t^* = 1.04$; (*b*) $t/t^* = 1.42$; (*c*) $t/t^* = 1.68$; (*d*) $t/t^* = 1.86$.

-0.0672) was conducted. These are two of the stronger waves in the simulation described above (figure 13*c*). The shape of the two-dimensional wave was obtained by solving the linearized Navier–Stokes equations. The eigenfunction of the + mode (parallel to the wave vector) of the oblique wave was similarly obtained using Squire's theorem. A full simulation was then conducted with these two eigenmodes and the laminar flow as the initial condition; no random disturbances were included. The initial amplitudes of the two modes were equal, and were chosen such that at the beginning of deceleration ($t = 5$ s), their magnitudes reach the level they do in the simulation with random disturbances (figure 13*c*). The − mode (perpendicular to the wave vector) of the oblique wave is established naturally. It gains energy from the interaction between the mean flow and the + mode.

Figure 16(*a*)–16(*d*) give the spectra at four times. At the beginning of deceleration (figure 16*a*), the two-dimensional and oblique waves have their linear shapes. At $t/t^* = 1.42$, they reach about the same level of energy as in figure 13(*c*), and nonlinear interactions begin to become significant (figure 16*b*). Since only two waves were seeded in this model simulation, nonlinear interaction occurs in a selective way (figure 16*c*). Initially the energy is in modes $[j, m] = [7, 0]$ and $[6, -1]$ (j and m are

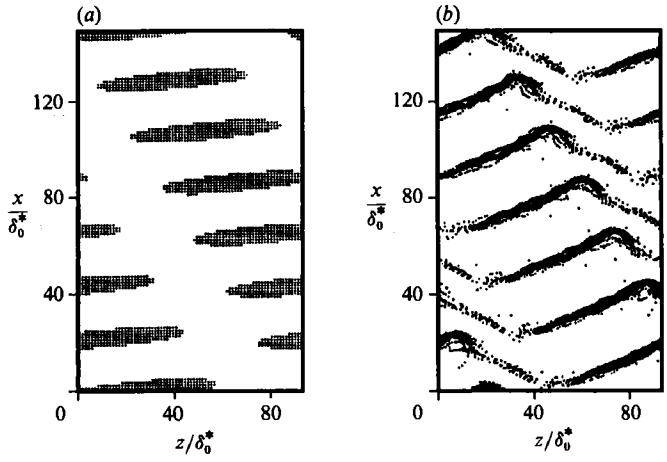

FIGURE 17. Flow visualization for model simulation. (a) $t/t^* = 1.16$; (b) $t/t^* = 1.90$.

the indices of streamwise and spanwise wavenumbers). The energy, even during nonlinear interactions, is trapped in modes that satisfy $j-m = 7l$ (where l is an integer). If two wave vectors belong to that family, so do their sum and difference. Thus, the final energy spectrum (figure 16*d*) shows an interesting feature; the energy is confined to ridges, oblique with respect to the k_z-axis. A less clean version of this phenomenon is observed in the simulation with random disturbances (figure 13*d*).

A passive-particle visualization of this model problem is presented in figure 17. At the time of deceleration, 9000 particles were released below the 'numerical laser sheet'. Sometime later (figure 17*a*), some particles are lifted upwards, revealing the interference pattern found in the preceding subsection (see figure 15*b*). Dislocation between the two patches of particles is obvious. Finally, Λ vortices appear (figure 17*b*). The tips of the Λ vortices are obliquely aligned as in the simulation with random disturbances (figure 8*c*).

This simple model provides an explanation of the prominent features of the full simulation with random initial disturbances. The choice of the initial dominant waves is arbitrary, and need not be limited to two. The choice of wavenumbers and the number of dominant waves was made to match a particular simulation with random disturbances. In both numerical simulations and laboratory experiments, the initial perturbation to the flow field determines these factors, and varies from realization to realization. Figure 18 supports this idea. Here, the energy (integrated in the normal direction) of six modes neighbouring the most unstable two-dimensional wave (and the two-dimensional wave itself) is shown as a function of time for the simulation with random initial disturbances. Although they had approximately the same energy at the beginning of simulation, they have been divided into two groups ('dominant' waves and 'less-dominant' waves) by the sorting-out process. The 'take-over' by the most unstable two-dimensional wave (0.294, 0) is noticeable. When nonlinear interaction becomes significant (around $t/t^* = 1.5$), the two waves ((0.294, 0) and (0.252, −0.0672)) which were selected for the model simulation dominate.

To show that the selection of dominant waves depends on the initial conditions two further simulations, which differ from the one studied above only in the random-number sequences used to generate the initial conditions, were performed; their passive-particle visualizations are shown in figures 19(*b*) and 19(*c*) along with the

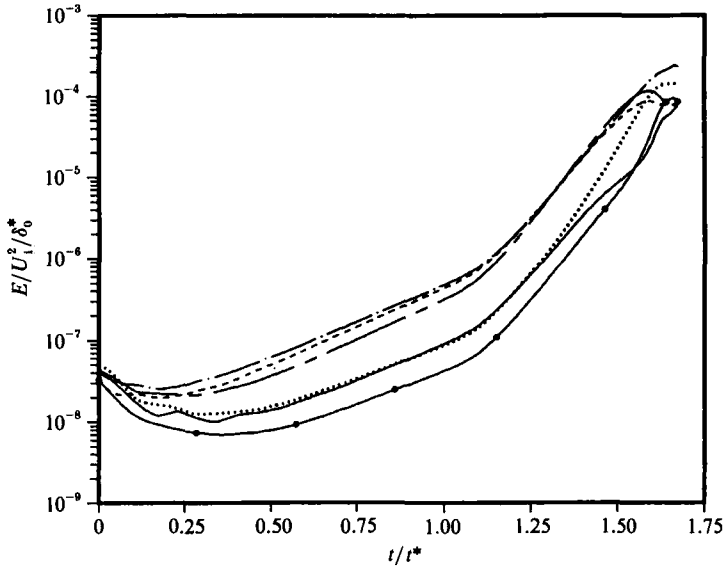

FIGURE 18. Energy history of typical six modes. ---, [6,0]; ——, [6,1]; -·-, [6,−1]; –··–, [7,0]; ···, [7,1]; ●, [7,−1].

earlier result (figure 19*a*). In figure 19(*b*), the tips of Λ vortices are obliquely aligned, but in the direction opposite to that in figure 19(*a*). In the case shown in figure 19(*c*), Λ vortices appear in a scattered pattern. When there are more than two dominant waves, the pattern becomes less regular. In fact, the energy spectrum corresponding to figure 19(*c*) shows that there are several important modes at the beginning of breakdown (figure 20).

In summary, unlike ribbon-induced transition (forced transition), the pattern of Λ vortices in natural transition arises from the presence of multiple dominant waves. The selection of waves that play important roles is determined by uncontrolled perturbations in the flow. Hence the control of natural transition should be much more difficult than that of ribbon-induced transition.

4.6. *Dependence on parameters*

One expects the onset and rapidity of transition to depend strongly upon the rate of deceleration. Figure 21 shows the growth of the most unstable two-dimensional waves ($k_x \delta_0^* = 0.294$) in full simulations with random disturbances for three different cases; $U_t/U_i = 0.56$, 0.75, 0.94. The other parameters ($R_{\delta_0^*}, t^* U_i/\delta_0^*$) remained unchanged. Obviously, stronger deceleration leads to earlier and quicker transition. However, we found that the patterns of the Λ vortices differ little in the three cases.

A simulation was conducted to investigate the effect of $R_{\delta_0^*}$. Figure 22 shows the flow visualization of a simulation in which $R_{\delta_0^*} = 1090$ (this is the value at $x = 1.0$ m, as opposed to $x = 0.62$ m), and U_t/U_i and t^* remained the same as in figure 8. The streamwise spacing of the Λ vortices (6.4 cm) is larger than in figure 8(*c*) (4.6 cm) because the streamwise wavelength of the most unstable two-dimensional wave is larger for high Reynolds numbers. The overall pattern of the Λ vortices is similar to that of the case described earlier.

The initial disturbance level is another parameter. Its effect is very similar to that of the rate of deceleration. Stronger perturbation leads to earlier transition, but there is no significant difference in the pattern of Λ vortices.

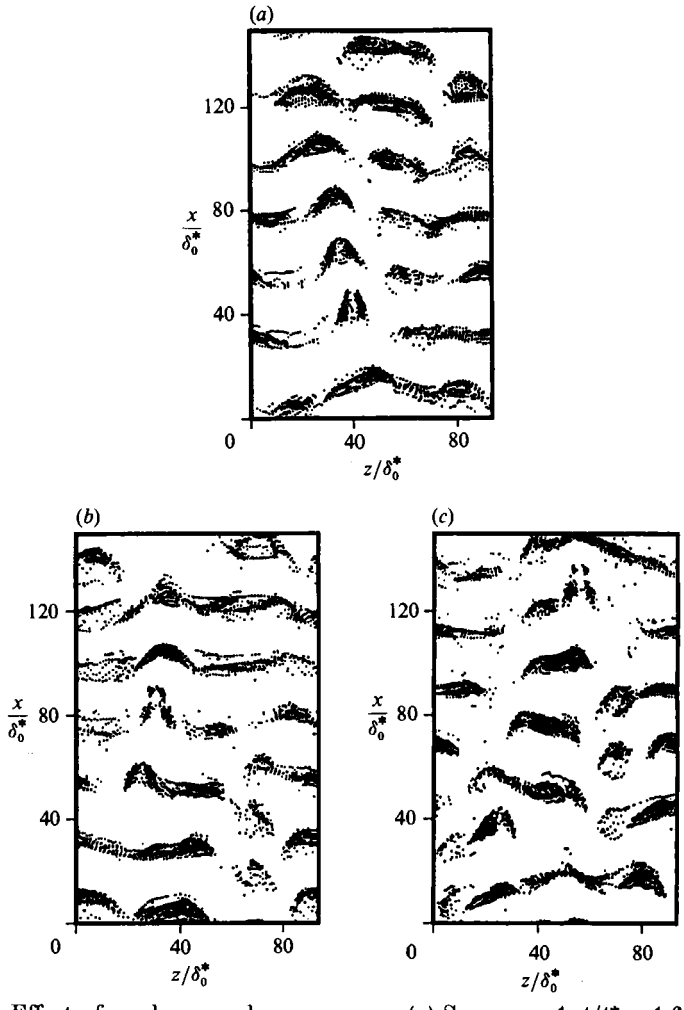

FIGURE 19. Effect of random-number sequences. (a) Sequence, 1, $t/t^* = 1.61$; (b) sequence 2, $t/t^* = 1.69$; (c) sequence 3, $t/t^* = 1.71$.

5. Simulations of the later stages of transition

In this section, the later stages of natural transition in a decelerating boundary layer are investigated using much higher numerical resolution (up to 6.29 million grid points). The behaviour of individual 'naturally-born' Λ vortices and of the flow structures is studied rather than the global patterns discussed in the previous section. All the available experimental studies of the later stages of transition used an artificial device (vibrating ribbon or rubber-sheet stimulator) to generate Λ vortices. All the numerical investigations of the later stages of transition (Wray & Hussaini 1984; Biringen 1984, 1987; Krist & Zang 1987) included a pair of oblique waves in addition to a dominant two-dimensional TS wave in the initial field, to create a clean Λ vortex. Hence, the evolving structure is symmetrical in z. It is important to scrutinize this approach because transition in most engineering flows is natural and not symmetrical. Therefore, our natural-transition results will be compared with a forced-transition experiment (Hama & Nutant 1963) to identify differences.

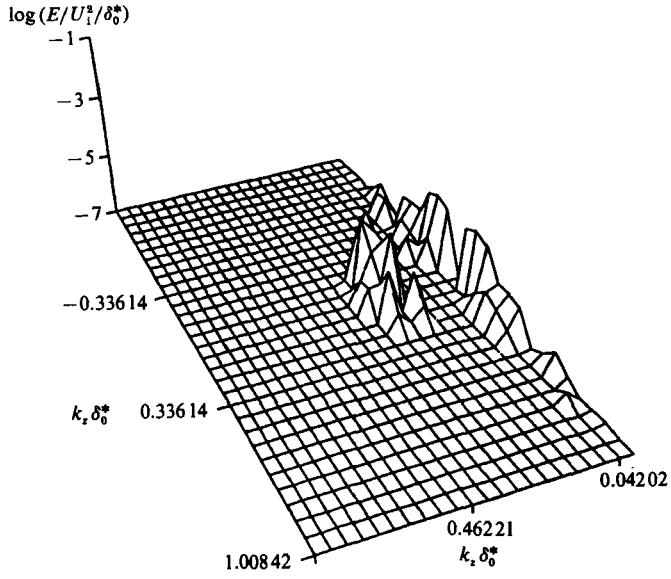

FIGURE 20. Energy spectrum, energy scale logarithmic, base 10, sequence 3, $t/t^* = 1.41$.

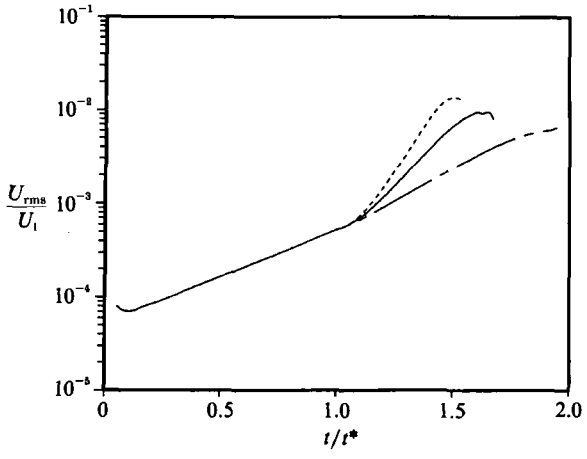

FIGURE 21. Most unstable two-dimensional waves. ---, $U_t/U_1 = 0.56$; ——, $U_t/U_1 = 0.75$; – – –, $U_t/U_1 = 0.94$.

5.1. *Choice of parameters*

Since we are interested in the development of an individual flow structure, we can reduce the size of the computational box to allow finer numerical resolution. Decreasing the Reynolds number ($R_{\delta_0^*}$) further eases the task because the eddies are not as small as their counterparts at high Reynolds number. We chose

$$R_{\delta_0^*} = 607 \ (x = 0.311 \text{ m}), \quad k_{x_0}\delta_0^* = 0.298, \quad \text{and} \quad k_{z_0}\delta_0^* = 0.0953.$$

With these values, the streamwise and the spanwise sizes of the new computational box become about 21 times and 66 times the initial displacement thickness (δ_0^*), respectively. From linear stability analysis, one can show that only one Λ vertex will

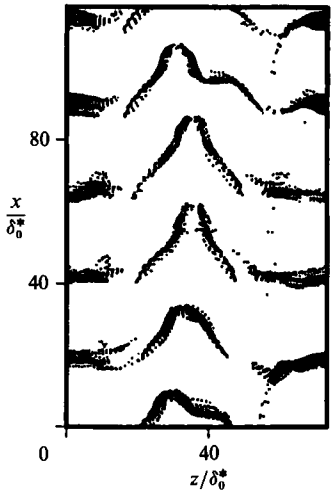

FIGURE 22. Effect of Reynolds number, $R_{\delta_0^*} = 1090$.

be contained in this box. Nevertheless, our simulation still begins with random noise and is more realistic than the previous ones (Wray & Hussaini 1984; Biringen 1984, 1987; Krist & Zang 1987), and it is fair to compare it with Hama & Nutant (1963).

Since the Reynolds number is somewhat low (but above the critical Reynolds number), the growth rate of the most unstable two-dimensional wave is smaller than in the preceding case. To compensate, we increase the rate of deceleration ($U_f/U_i = 0.5$), but not enough to cause flow reversal. Under these conditions, Λ vortices appear around $t/t^* = 1.602$.

The numerical resolution is refined as the flow evolves. Additional grid points are introduced whenever the ratio of the energy of the weakest mode to that of the most energetic mode approaches 10^{-6}. This means that the truncation error in the primitive variables is no more than 0.1%. A smooth fall-off of the energy at the highest wavenumbers is also ensured. The maximum number of grid points used, $96 \times 128 \times 512$, is enough to resolve structures in a fully developed turbulent flow at this Reynolds number. The streamwise and spanwise spacing between grid points are $\Delta x^+ = 2.4$ and $\Delta z^+ = 1.4$ in wall units (based on the mean wall stress at $t/t^* = 1.625$). In the normal direction, the grid points are clustered near the wall, and the first grid point is located at $y^+ = 0.0012$.

5.2. *Results and discussion*

5.2.1. *Flow visualization*

A 'hydrogen-bubble' simulation is shown in figure 23. Two hundred bubbles were released on a vertical line in the peak plane ($z/\delta_0^* = 35.3$) at evenly-spaced times ($\Delta t = 0.001t^*$). Although the flow is periodic in the x- and z-directions, bubbles which leave the computational box are discarded. A high-shear layer near $y/\delta_0^* = 2.3$ exists at the first time shown (figure 23*a*). From the numerical point of view, the steep gradient far from the wall causes trouble as the flow evolves because the grid points are clustered near the wall; the grid is not designed to capture the high-shear layer. A kink in the high-shear layer is clearly seen in figure 23(*b*) (see the arrow), and a concentrated vortex later develops at that location (figure 23*c–e*). These processes occur in a time much shorter than the duration of the linear stage; note the times given on the figures. This simulation is in good agreement with the experiment of

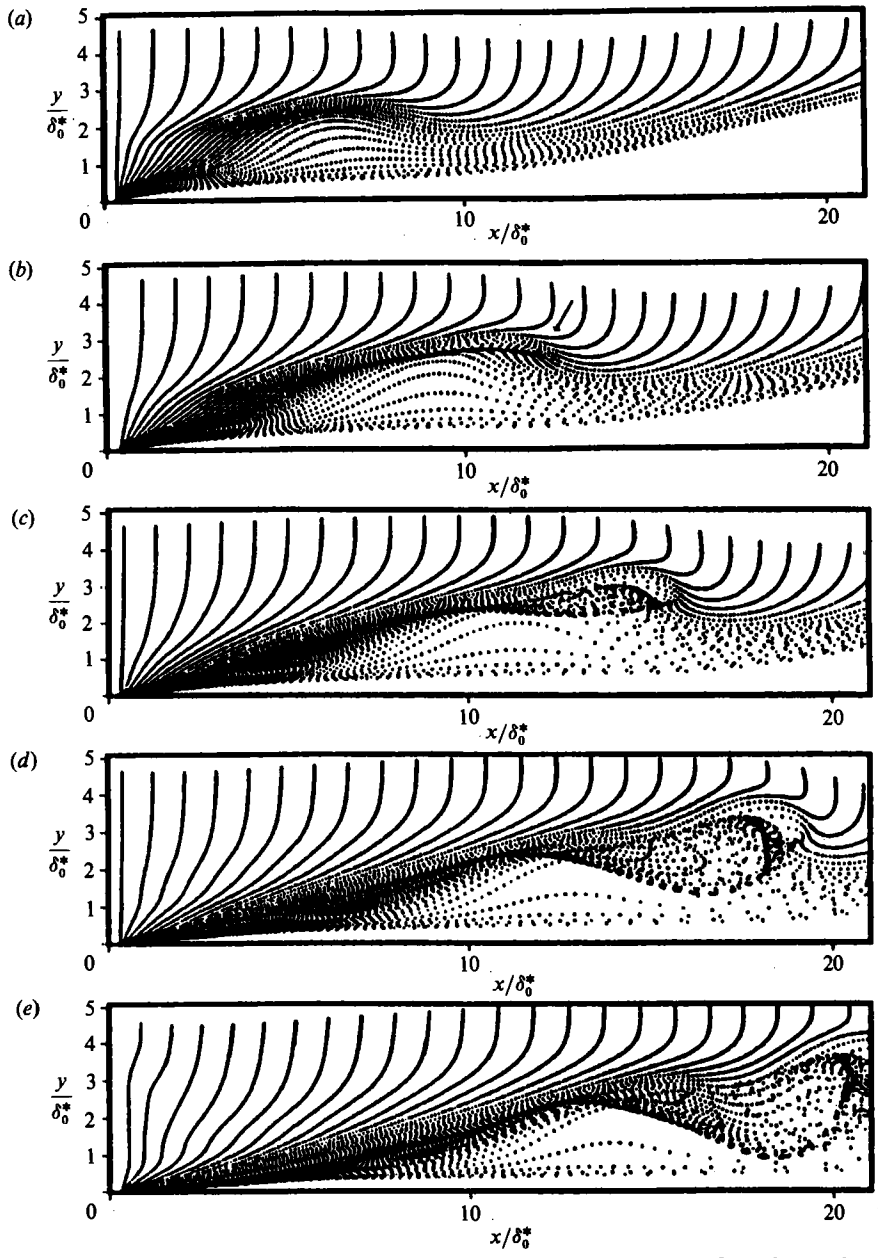

FIGURE 23. Hydrogen-bubble simulation. Bubbles are released in the peak plane. (*a*) $t/t^* = 1.6021$; (*b*) 1.6098, (*c*) 1.6161, (*d*) 1.6221, (*e*) 1.6266.

Hama & Nutant (1963); compare figure 23 with their figure 13. They regarded the formation of a concentrated vortex as part of the breakdown process. Each of their frames corresponds very well to one of ours except the last one for which the numerical resolution may be insufficient (see below). Zang (1987, private communication) has shown that better agreement between the simulation and Hama & Nutant's experiment is obtained if the 'bubble wire' is displaced slightly from the peak plane.

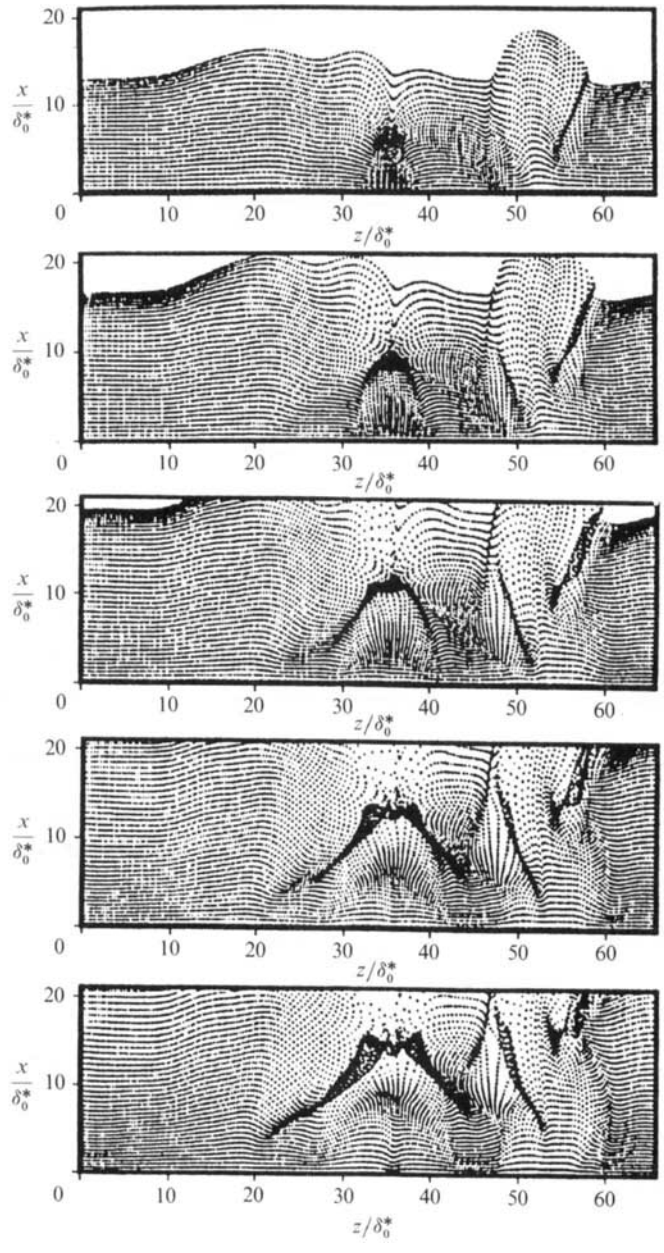

FIGURE 24. Hydrogen-bubble simulation. Bubbles are released at $y/\delta_0^* = 1.32$. (*a*) $t/t^* = 1.6021$; (*b*) 1.6098, (*c*) 1.6161, (*d*) 1.6221, (*e*) 1.6266.

Figure 24 shows a simulation of a horizontal hydrogen-bubble wire. Two hundred bubbles were released on a spanwise line at $y/\delta_0^* = 1.32$, at the same release times as in figure 23. The formation of a Λ vortex is clearly visible. Retarded particles near $x/\delta_0^* = 14$ and $z/\delta_0^* = 35$ indicate the formation of a high-shear layer. There is a close resemblance between the Λ vortex in our simulation and the one in the experiment of Hama & Nutant (1963). See their figure 11(*a*).

Since the experiment was artifically controlled by a rubber-sheet stimulator, the agreement between the experiment and the simulation strongly suggests that in two-

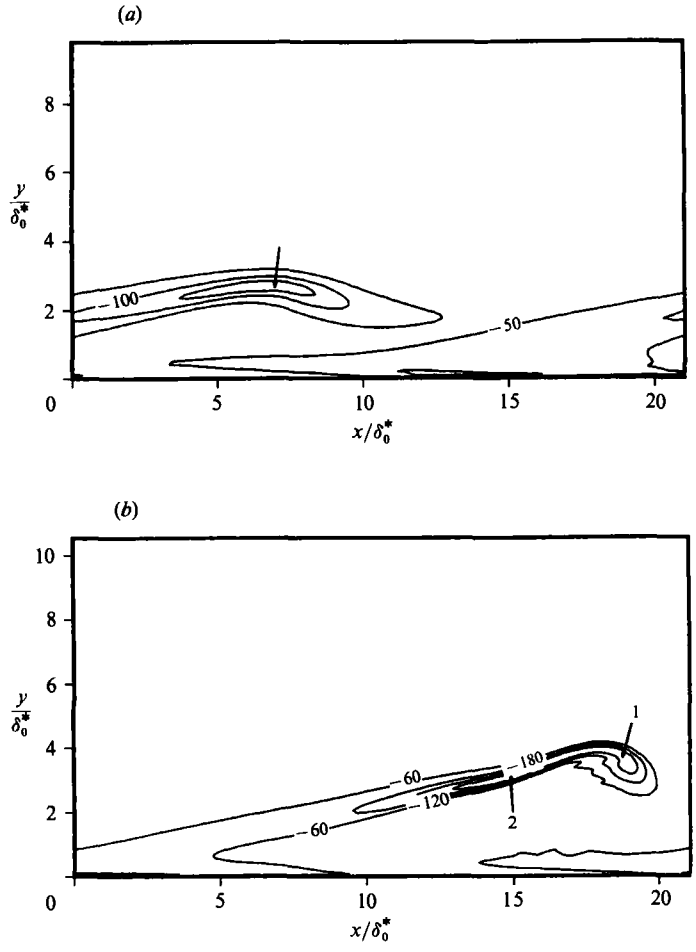

FIGURE 25. ω_z contours in the peak plane. (*a*) $t/t^* = 1.6021$, increment, $-50\ \mathrm{s}^{-1}$; (*b*) $t/t^* = 1.6221$, increment, $-60\ \mathrm{s}^{-1}$.

dimensional boundary layers and in the absence of by-pass mechanisms the formation of Λ vortices and high-shear layers and their subsequent breakdown to smaller scales are universal steps toward turbulence, and that the processes are identical in natural and in forced transition.

5.2.2. *Vortical structure*

As noted by many previous authors, the high-shear layer is an important feature of the later stages of development of this flow. It is created by the lifting of low-speed fluid that originates near the wall by the upwelling flow between the legs of the Λ vortex. After the low-speed fluid is lifted above the Λ vortex, it is stretched in the spanwise direction as the vortex-induced flow turns; as a result, the high-shear layer is slightly thicker near the centre (peak) plane of the Λ vortex than at the edges. As the lifted fluid has lower velocity than the head of the Λ vortex, it is left behind the latter. Thus, the upstream part of the high-shear layer contains the fluid that was lifted first; this fluid has also been stretched laterally for a longer period. Since the upstream sections of the legs of the Λ vortex are also farther apart than the downstream ones, the upstream part of the high-shear layer is both wider and

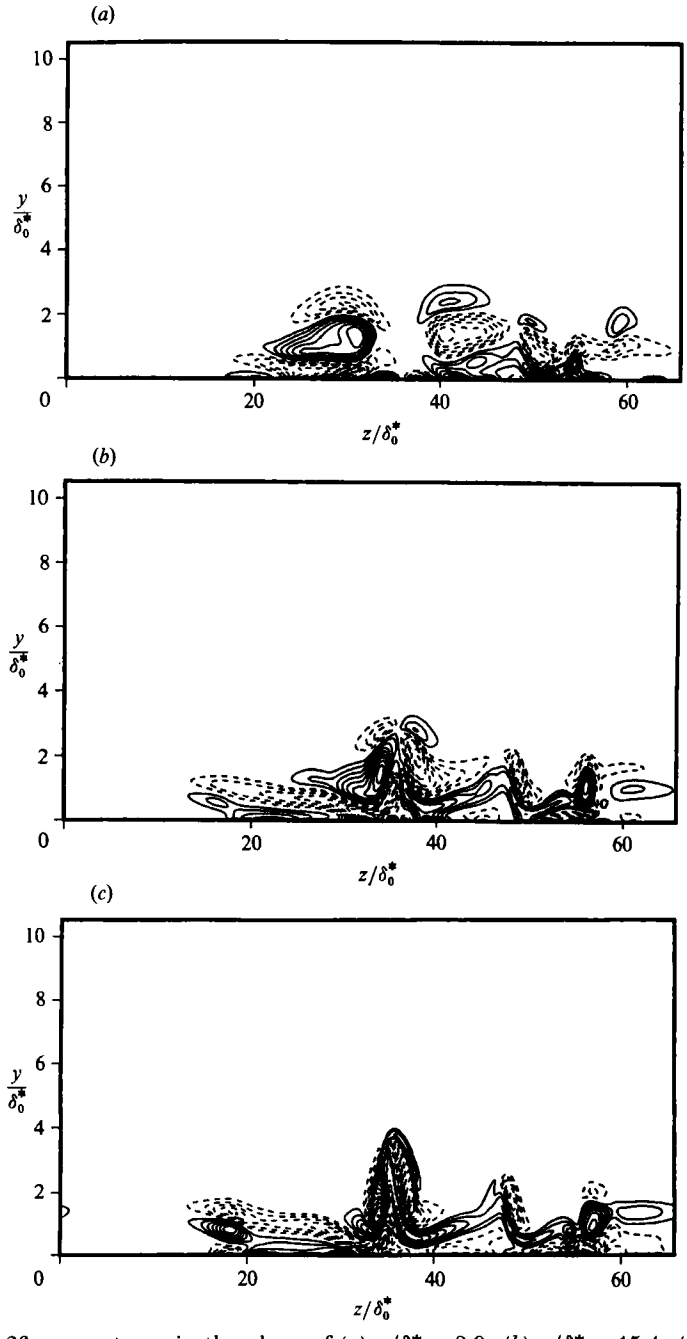

FIGURE 26. ω_x contours in the plane of (a) $x/\delta_0^* = 8.9$; (b) $x/\delta_0^* = 15.4$; (c) $x/\delta_0^* = 18.6$, increment, $-10\ \mathrm{s}^{-1}$.

thinner than the forward section. These motions give the high-shear layer a characteristic arrowhead shape; in a plan view, the arrowhead lies within the pocket of the Λ vortex.

The high-shear layer can be regarded as a short vortex sheet. Consequently, it is more susceptible to roll-up at its forward and aft ends than to the Kelvin–Helmholtz type of instability associated with longer vortex sheets; the forward (downstream)

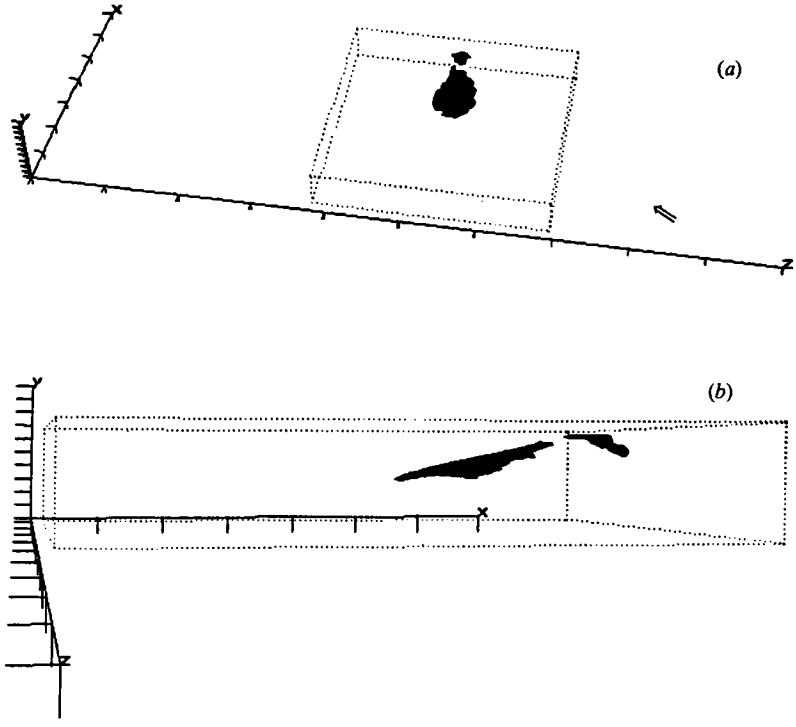

FIGURE 27. ω_z-contour surface, $t/t^* = 1.6221$. (*a*) Perspective view; (*b*) side view.

end is a more likely site for the initiation of roll-up as the vorticity is more concentrated there. At a later time, the roll-up causes the forward section of the high-shear layer to bend downward. At the same time, the combination of roll-up and stretching thins the vortex sheet and causes it to have two vorticity maxima; this is illustrated in figure 25 which shows contour plots of spanwise vorticity in the peak plane at $t/t^* = 1.6021$ and $t/t^* = 1.6221$, corresponding to parts (*a*) and (*d*) of figures 23–24. Zero contours are not shown for clarity. Figure 25(*a*) contains only one maximum in the magnitude of ω_z; it occurs in the high-shear layer at the location indicated by an arrow. This figure also shows the downwrd bending of the front part of the high-shear layer which later becomes the kink of figure 23(*b*). Figure 25(*b*) shows that ω_z later develops a second maximum. The locations of the two maxima are indicated by the two arrows. The original maximum (arrow 1) has been convected downstream and lifted upwards (it is now outside the boundary layer), the second local maximum appears in the upstream part of the high-shear layer and gains strength (arrow 2). The location of the original maximum (arrow 1) matches the tip region of the *A* vortex (see figure 28). Thus, one can deduce that the upstream maximum value (arrow 2) is an indication of the shear-layer instability. This is the two-spike stage. Although the simulation was stopped shortly after this time, it is important to note that a vortex sheet with two vorticity maxima will tend to roll up at two distinct locations, leading to a pattern typical of the so-called three-spike stage. Still later, these processes will result in the shear-layer rolling up in more and more complex patterns, in the production of additional maxima in the vorticity and, eventually, to the characteristic multi-spike patterns that have been observed. From figures 25 and 23(*d*), one can deduce that the high-shear layer rolls up into a concentrated vortex at the tip region. It is not difficult to conjecture that the

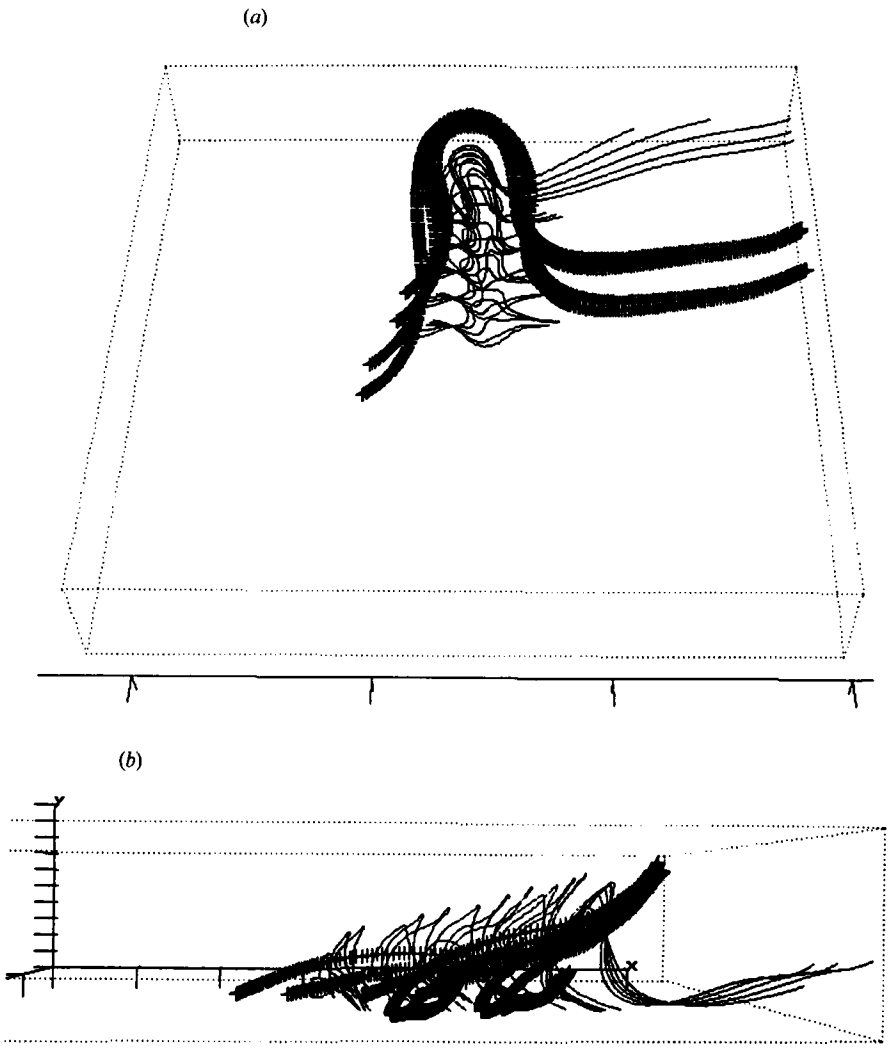

FIGURE 28. Vortex lines at $t/t^* = 1.6221$. (*a*) Perspective view; (*b*) side view.

upstream high-ω_z region (arrow 2) in figure 25(*b*) will evolve into another concentrated vortex like the second roll-up in the experiment (part (*e*) in figure 13 of Hama & Nutant 1963).

Contour plots of streamwise vorticity (ω_x) at $x/\delta_0^* = 8.9$, 15.4, and 18.6 are given in figures 26(*a*)–26(*c*), respectively, corresponding to $t/t^* = 1.6266$. The solid and the dashed lines represent negative and positive values, respectively. In these figures, cross-sections of the primary vortices and the secondary ones below them are clearly seen. Note that the vortical structure is inclined to the plate with the tip region being highest. Near $z/\delta_0^* = 55$, a strong streamwise vortex is present. Above the primary *A* vortex, a relatively weak pair of vortices is found. Also one can see the beginning of formation of small-scale structures very near the wall.

Three-dimensional vortical structures are shown in perspective in figures 27–29. The flow is in the x-direction. Figures 27 and 28 correspond to part (*d*) of figures 23 and 24, and figure 29 corresponds to part (*e*) of figures 23 and 24. Since it is not possible to display the entire flow database at one time, only the data for the part

FIGURE 29. Vortex lines at $t/t^* = 1.6266$.

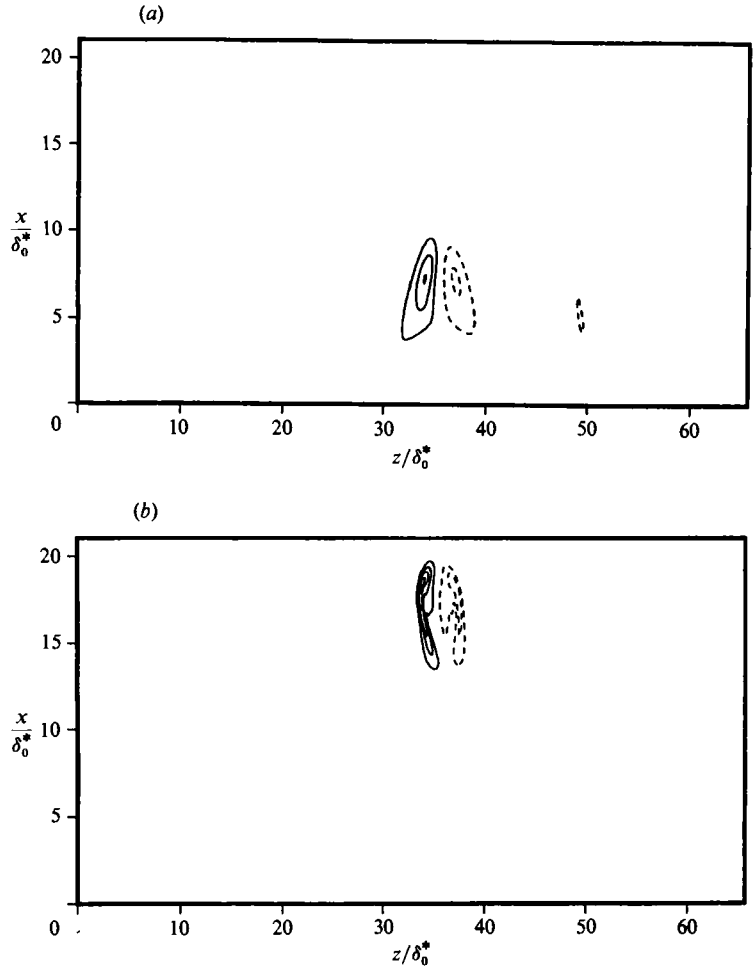

FIGURE 30. ω_y contours in a horizontal plane, ——, negative; ---, positive. (*a*) $t/t^* = 1.6021$, $y/\delta_0^* = 2.3$, increment, 20 s^{-1}; (*b*) $t/t^* = 1.6221$, $y/\delta_0^* = 2.8$, increment, 40 s^{-1}.

of the domain represented by the dotted box (using every other point in each coordinate direction) were used for the plots. In figures 27 and 28, the dotted box covers the entire range of x, $1.04\delta_0^* \leqslant y \leqslant 4.39\delta_0^*$, and $25.2\delta_0^* \leqslant z \leqslant 45.9\delta_0^*$. Figure 29 covers the same ranges in x and y as figure 27, but only $27.6\delta_0^* \leqslant z \leqslant 43.0\delta_0^*$ in z. Figure 27 shows the ω_z-contour surface of -175 s^{-1}. Part (*b*) is an enlarged side view of part (*a*) (see the arrow for the view point). The high-shear layer has been distorted (figure 27*a*), and no longer has the arrowhead shape (see figure 9*f*). The downstream part of the high-shear layer is bent downwards (figure 27*b*). The separation of the high-shear layer into two parts indicates the presence of two local vorticity maxima as shown in figure 25(*b*). This supports the idea of vortex roll-up mentioned earlier.

The process described in the beginning of this subsection can also be regarded as one in which the originally horizontal spanwise vortex lines representing the shear layer near the wall are lifted. Figure 28(*a*) shows vortex lines in a perspective view. The thick lines represent the Λ vortex which looks like a hairpin at this time. Owing to the velocity field associated with the Λ vortex, originally horizontal vortex lines near the plate (indicated by the thin lines) are pulled upwards between the legs of the Λ vortex, and then stretched in the spanwise direction. This leads to the flat heads of the vortex lines representing the high-shear layer formed above the Λ vortex. Vortex lines are attached to the walls of the dotted box. As they cannot break during lift-up, the lifting process leaves walls of vertical vorticity connecting the high-shear layer near the top of the boundary layer to the low-speed fluid at the base of the boundary layer on either side. This vertical vorticity represents thin shear layers (with large values of $\partial u/\partial z$) that lie just inside the legs of the Λ vortex. Figure 28(*b*) shows a side view of figure 28(*a*). The pulled vortex lines lean forward owing to acceleration of the fluid as it is lifted; a line connecting their tops is inclined at an angle well-matched to that of ω_z contours (figure 25*b*).

Vortex lines of the Λ vortex are shown at a later time in figure 29; it has become a hairpin (Ω-shaped) vortex. It would be interesting to see whether a vortex ring like the one described in Moin, Leonard & Kim (1986) pinches off at a later time; it is possible that chaotic breakdown occurs first. The evolution of Λ vortices into Ω vortices was also observed experimentally by Hama & Nutant (1963).

The behaviour of the vertical shear layers is shown in figure 30 which gives contour plots of the vertical component of vorticity (ω_y) in a horizontal (x,z)-plane in the strong-ω_y region. Figure 30(*a*) corresponds to $t/t^* = 1.6021$ at $y/\delta_0^* = 2.3$, and figure 30(*b*) to $t/t^* = 1.6221$ at $y/\delta_0^* = 2.8$. The front portions of the thin vertical shear layers roll up in much the same way as the horizontal high-shear layer.

Nearly all of the features that have been observed experimentally are explained by the physical model just described. The processes are the same as those associated with artificially-produced transition (Kovasznay *et al.* 1962; Wray & Hussaini 1984); compare Wray & Hussaini's figure 5 with our figure 25. It is worth adding that these processes probably amplify small disturbances that destroy the symmetry of the Λ vortex and lead, after a short time, to the chaotic patterns associated with fully turbulent flow.

5.2.3. *Discussion*

The formation of very steep velocity gradients away from the plate causes trouble for the numerical method because the grid points are clustered tightly near the wall. We made higher-resolution runs in an attempt to resolve the further development of the flow structure, but were able to simulate only very little of the further development. A correct tendency towards multi-spike stages was found. However, vorticity contour plots showed signs of poor numerical resolution. To resolve the high-shear layer far from the wall properly, an adaptive-grid method is probably the best approach. The resolution in the other two directions, especially spanwise, is also heavily taxed.

Although we considered a single Λ vortex in this section, similar physics was found in simulations in which multiple Λ vortices were present in the computational box.

6. Concluding remarks

Laminar–turbulent transition in a decelerating flat-plate boundary layer has been investigated by direct numerical solution of the full Navier–Stokes equations. The mean velocity was assumed parallel to the plate, periodic boundary conditions were applied, and correct mean-velocity profiles were maintained by way of a body force. Small-amplitude white random noise was included in the initial conditions to eliminate bias in selecting which modes are amplified.

In the early stages of transition, two-dimensional and/or slightly oblique waves initially grow because of an inflexional instability. Their subsequent nonlinear interactions trigger the breakdown and determine the pattern of the Λ vortices. The results are in good agreement with flow-visualization experiments (GH). The tips of the Λ vortices are rarely aligned in the flow direction, and they appear in local patches in space, often near the dislocation in the initial wave pattern. A simple wave-interference model accounting for these features of natural transition has been developed. It suggests that owing to interference among multiple waves amplified at the linear stage of natural transition, the peak perturbations are not necessarily aligned normal to the flow direction, and occur locally in space. Since breakdown occurs where the primary instability is strong, the model explains the observed pattern of the Λ vortices. This model was tested numerically, and the resultant pattern of the Λ vortices showed features found in the full simulation. It was also demonstrated that the selection of dominant waves is governed by small differences in the unpredictable initial disturbances.

The later stages of transition were studied with higher numerical resolution. Our results indicate that the naturally-born Λ vortices undergo breakdown processes similar to those of ribbon-induced Λ vortices. The breakdown of high-shear layers into concentrated vortices and the subsequent evolution of Ω vortices observed in forced-transition experiments (Hama & Nutant 1963) are also detected in our simulation. It was shown that a shear-layer instability (sometimes called the tertiary instability) appears in the upstream part of the high-shear layer; it resembles a vortex-sheet roll-up and explains the development of the multiple-spike stages. To proceed to the terminal stages of breakdown, one needs to be able to resolve the high-shear layers away from the wall.

The authors gratefully acknowledge useful discussions with Professor Helen Reed of Arizona State University during the course of this work.

NASA-Ames Research Center has provided the computer time for this research under Cooperative Agreement NCC2-15. Financial support for the investigators (except P.R.S.) was provided through AFOSR grant AF-84-0083.

Appendix. Mathematical equivalence of decelerating-plate and decelerating-free-stream flows

In this Appendix, it will be demonstrated that the governing equations and boundary conditions for the decelerating-plate problem can be reduced to those of the decelerating-free-stream problem using a reference frame moving with the plate (it is not a Galilean reference frame because the plate is decelerating). Both independent and dependent variables are transformed with respect to the reference frame.

Let primed variables be those in the inertial (laboratory) reference frame, and

unprimed variables be those in the moving reference frame. Prandtl's boundary-layer equations (Schlichting 1979) for a two-dimensional decelerating-plate problem, along with the continuity and the initial and boundary conditions, read

$$\frac{\partial U'}{\partial t'}+U'\frac{\partial U'}{\partial x'}+V'\frac{\partial U'}{\partial y'}=\nu\frac{\partial^2 U'}{\partial y'^2}, \tag{A 1}$$

$$\frac{\partial U'}{\partial x'}+\frac{\partial V'}{\partial y'}=0, \tag{A 2}$$

$$U'=-U_{\mathrm{IB}}(x',y') \quad \text{at } t'=0, \tag{A 3}$$

$$U'=-U_{\mathrm{w}}(t') \quad \text{at } y'=0, \tag{A 4}$$

$$V'=0 \quad \text{at } y'=0, \tag{A 5}$$

$$U'\to 0 \quad \text{as } y'\to\infty, \tag{A 6}$$

where U_{IB} is the inverted Blasius profile, and U_{w} is the speed of the plate. The pressure is assumed constant throughout the flow field. It is important to note that (A 1)–(A 6) are valid on only $x'\in[x'_{\mathrm{le}}, x'_{\mathrm{le}}+L]$. Here, $x'_{\mathrm{le}}(t')$ is the position of the leading edge of the plate at a given time, t'. Thus,

$$U'(x',0,t')=\frac{\mathrm{d}x'_{\mathrm{le}}}{\mathrm{d}t'}=-U_{\mathrm{w}}(t'). \tag{A 7}$$

The new variables with respect to the moving reference frame are defined as

$$x=x'-x'_{\mathrm{le}}(t'), \quad y=y', \quad t=t', \quad U=U'+U_{\mathrm{w}}(t'), \quad V=V'. \tag{A 8}$$

Introducing the new variables defined above, and using the chain rule, one can obtain

$$\frac{\partial U'}{\partial x'}=\frac{\partial U}{\partial x}, \quad \frac{\partial U'}{\partial y'}=\frac{\partial U}{\partial y}, \quad \frac{\partial^2 U'}{\partial y'^2}=\frac{\partial^2 U}{\partial y^2}, \quad \frac{\partial V'}{\partial y'}=\frac{\partial V}{\partial y}. \tag{A 9}$$

For the unsteady term, it can be shown that

$$\begin{aligned}\frac{\partial U'}{\partial t'}&=\frac{\partial U'}{\partial x}\frac{\partial x}{\partial t'}+\frac{\partial U'}{\partial y}\frac{\partial y}{\partial t'}+\frac{\partial U'}{\partial t}\frac{\partial t}{\partial t'}\\&=U_{\mathrm{w}}(t)\frac{\partial U'}{\partial x}+\frac{\partial U'}{\partial t}\\&=U_{\mathrm{w}}(t)\frac{\partial U}{\partial x}+\frac{\partial U}{\partial t}-\frac{\mathrm{d}U_{\mathrm{w}}(t)}{\mathrm{d}t}.\end{aligned} \tag{A 10}$$

Substituting (A 9) and (A 10) into (A 1)–(A 6), one gets the following set of governing equations and initial and boundary conditions,

$$\frac{\partial U}{\partial t}+U\frac{\partial U}{\partial x}+V\frac{\partial U}{\partial y}=\frac{\mathrm{d}U_{\mathrm{w}}}{\mathrm{d}t}+\nu\frac{\partial^2 U}{\partial y^2}, \tag{A 11}$$

$$\frac{\partial U}{\partial x}+\frac{\partial V}{\partial y}=0, \tag{A 12}$$

$$U=U_{\mathrm{B}}(x,y) \quad \text{at } t=0, \tag{A 13}$$

$$U=V=0 \quad \text{at } y=0, \tag{A 14}$$

$$U\to U_{\mathrm{w}}(t) \quad \text{as } y\to\infty. \tag{A 15}$$

Equations (A 11)–(A 15) are valid on $x \in [0, L]$. This new formulation represents a decelerating-free-stream problem, if $U_w(t)$ is interpreted as the velocity of the freestream ($U_\infty(t) = U_w(t)$). Then dU_w/dt is an effective pressure gradient.

REFERENCES

BARRY, M. D. J. & ROSS, M. A. S. 1970 The flat-plate boundary layer. Part 2. The effect of increasing thickness on stability. *J. Fluid Mech.* **43**, 813–818.

BETCHOV, R. 1960 On the mechanism of turbulent transition. *Phys. Fluids* **3**, 1026.

BIRINGEN, S. 1984 Final stages of transition to turbulence in plane channel flow. *J. Fluid Mech.* **148**, 413–442.

BIRINGEN, S. 1987 Three-dimensional vortical structures of transition in plane channel flow. *AIAA Paper* 87-0046.

CRAIK, A. D. D. 1971 Nonlinear resonant instability in boundary layers. *J. Fluid Mech.* **50**, 393–413.

DRAZIN, P. & REID, W. 1981 *Hydrodynamic Stability*. Cambridge University Press.

FALES, E. N. 1955 A new laboratory technique for investigation of the origin of fluid turbulence. *J. Franklin Inst.* **259**, 491–515.

FASEL, H. 1976 Investigation of the stability of boundary layers by a finite-difference model of the Navier–Stokes equations. *J. Fluid Mech.* **78**, 355–383.

FASEL, H., KONZELMANN, U. & RIST, U. 1986 Numerical simulation of three-dimensional, spatially amplified disturbances in a flat plate boundary layer. In *Bull. Am. Phys. Soc.* November, 1679.

GAD-EL-HAK, M. & DAVIS, S. H. 1982 Study of effects of acceleration/deceleration on turbulence and transition. *Flow Res. Rep.* 217.

GAD-EL-HAK, M., DAVIS, S. H., MCMURRAY, J. T. & ORSZAG, S. A. 1984 On the stability of the decelerating laminar boundary layer. *J. Fluid Mech.* **138**, 297–323.

GASTER, M. 1962 A note on the relationship between temporally increasing and spatially increasing disturbances in hydrodynamic stability. *J. Fluid Mech.* **14**, 222–224.

GASTER, M. 1980 On wave packets in laminary boundary layers. In *Proc. of IUTAM Symp. on Laminar–Turbulent Transition*. Springer.

GREENSPAN, H. P. & BENNEY, D. J. 1963 On shear-layer instability, breakdown and transition. *J. Fluid Mech.* **15**, 133–153.

HAMA, F. R. & NUTANT, J. 1963 Detailed flow-field observations in the transition process in a thick boundary layer. In *Proc. 1963 Heat Transfer and Fluid Mechanics Institute*, pp. 77–93. Stanford University Press.

HEGARTY, J. C. 1958 Investigation of transition caused by the stopping of a flat plate. *AFOSR TN*58-627.

HERBERT, TH. 1984 Analysis of the subharmonic route to transition in boundary layers. *AIAA Paper* 84-0009.

HERBERT, TH. 1985 Three-dimensional phenomena in the transitional flat-plate boundary layer. *AIAA Paper* 85-0489.

HERBERT, TH. 1988 Secondary instability of boundary layers. *Ann. Rev. Fluid Mech.* **20**, 487–526.

KACHANOV, Y. S. & LEVCHENKO, V. Y. 1984 The resonant interaction of disturbances at laminar–turbulent transition in a boundary layer. *J. Fluid Mech.* **138**, 209–247.

KLEBANOFF, P. S., TIDSTROM, K. D. & SARGENT, L. M. 1962 The three-dimensional nature of boundary-layer instability. *J. Fluid Mech.* **12**, 1–34.

KLEISER, L. & LAURIEN, E. 1985 Three-dimensional numerical simulation of laminar–turbulent transition and its control by periodic disturbances. In *Laminar–Turbulent Transition, Proc. 2nd IUTAM Symp., Novosibirsk* (ed. V. V. Kozlov). Springer.

KLEISER, L. & ZANG, T. A. 1991 Numerical simulation of transition in wall-bounded shear flows. *Ann. Rev. Fluid Mech.* **23**, 495–537.

KOVASZNAY, L. S. G., KOMODA, H. & VASUDEVA, B. R. 1962 Detailed flow field in transition. In *Proc. 1962 Heat Transfer and Fluid Mechanics Institute*, pp. 1–26. Stanford University Press.

KRIST, S. E. & ZANG, T. A. 1987 Numerical simulation of channel flow transition – Resolution requirements and structure of the hairpin vortex. *NASA Tech. Paper* 2667.

LAURIEN, E. & KLEISER, L. 1985 Active control of Tollmien–Schlichting waves in the Blasius boundary layer by periodic wall suction. In *Proc. 6th GAMM Conf. on Numerical Methods in Fluid Dynamics, Göttingen, September 25–27, 1985*. Vieweg.

LEONARD, A. & WRAY, A. 1982 A new numerical method for the simulation of three-dimensional flow in a pipe. In *8th Intl Conf. on Numerical Methods in Fluid Dynamics, Aachen, W. Germany, June 1982*.

LING, C. H. & REYNOLDS, W. C. 1973 Non-parallel flow corrections for the stability of shear flows. *J. Fluid Mech.* **59**, 571–591.

MOIN, P., LEONARD, A. & KIM, J. 1986 Evolution of a curved vortex filament into a vortex ring. *Phys. Fluids* **29**, 955–963.

NISHIOKA, M. & ASAI, M. 1985 Three-dimensional wave-disturbances in plane Poiseuille flow. In *Laminar–Turbulent Transition, Proc. 2nd IUTAM Symp., Novosibirsk* (ed. V. V. Kozlov), pp. 173–182. Springer.

ORSZAG, S. A. & PATERA, A. T. 1983 Secondary instability of wall-bounded shear flows. *J. Fluid Mech.* **128**, 347–385.

REYNOLDS, O. 1883 An experimental investigation of the circumstances which determine whether the motion of water shall be direct or sinuous, and of the law of resistance in parallel channels. *Phil. Trans. R. Soc. Lond.* **174**, 935–982.

SARIC, W. S., KOZLOV, V. V. & LEVCHENKO, V. Y. 1984 Forced and unforced subharmonic resonance in boundary-layer transition. *AIAA Paper* 84-0007.

SARIC, W. S. & NAYFEH, A. H. 1975 Nonparallel stability of boundary-layer flows. *Phys. Fluids* **18**, 945–950.

SCHLICHTING, H. 1979 *Boundary Layer Theory*, 7th edn. McGraw-Hill.

SINGER, B. A., FERZIGER, J. H., SPALART, P. R. & REED, H. L. 1987 Local intermodal energy transfer of the secondary instability in a plane channel. *AIAA Paper* 87-1202.

SPALART, P. R., MOSER, R. D. & ROGERS, M. M. 1991 Spectral methods for the Navier–Stokes equations with one infinite and two periodic directions. *J. Comp. Phys.* **96**, 297–324.

SPALART, P. R. & YANG, K. S. 1987 Numerical study of ribbon-induced transition in Blasius flow. *J. Fluid Mech.* **178**, 345–365.

THOMAS, A. S. W. 1983 The control of boundary-layer transition using a wave-superposition principle. *J. Fluid Mech.* **137**, 233–250.

WILLIAMS, D. R., FASEL, H. & HAMA, F. R. 1984 Experimental determination of the three-dimensional vorticity field in the boundary-layer transition process. *J. Fluid Mech.* **149**, 179–203.

WRAY, A. & HUSSAINI, M. Y. 1984 Numerical experiments in boundary-layer stability. *Proc. R. Soc. Lond.* A **392**, 373–389.